21. Nanoporous Metals

Yi Ding, Zhonghua Zhang

In this chapter, we mainly describe the fabrication, properties, and potential applications of nanoporous metals (NPMs) with random porous structure. Nanoporous metals represent an interesting type of nanostructured material with nanosized porosity and ultrahigh specific surface area, and thus possess unique mechanical, physical, and chemical properties associated with their nanoporous structure. Based upon the porosity distribution, nanoporous metals can be classified into two categories: one has a random porous structure, and the other has a regular pore distribution. Nanoporous metals with random porous structure can be synthesized by the dealloying strategy, whereas template methods are normally used to fabricate nanoporous metals with more regular pore distribution. Nanoporous metals date back to the days of Raney (1920s) when high specific surface metal catalysts were prepared by dealloying Al-based alloys in alkaline solutions. In the new century, monolithic nanoporous metals received renewed attention due to the observation of a series of very intriguing structural properties. Nanoporous metals made by dealloying exhibit a three-dimensional bicontinuous interpenetrating ligament (metal)–channel (void) structure with a length scale of several nanometers to hundreds of nanometers, and the characteristic size can be modulated to as large as several microns by treatments such as thermal annealing. In contrast, the template technique can precisely control the pore size and microstructure of nanoporous metals, but dynamic modulation of the dominant length scale is virtually impossible. In addition, nanoporous metals are different from metallic foams, which have a length scale of several microns to more than 1 cm, and are normally used as damping and acoustic materials. Here, we mainly focus on dealloyed nanoporous metals. Firstly, the dealloying method and formation mechanism of nanoporous metals are reviewed based upon previous experimental observations and computer simulation. Secondly, we summarize recent knowledge on microstructures of nanoporous metals and their unique properties (catalytic, electrocatalytic, mechanical, sensing, optical, etc.). Finally, potential applications of nanoporous metals are discussed in the fields of fuel cells, catalysis, sensors, actuators, etc.

21.1 Preparation of Nanoporous Metals

Many routes have been reported to prepare nanoporous metals, including transmetallation (galvanic replacement) reaction [21.1–3], the combination of block-copolymer template with deposition [21.4], chem-

R. Vajtai (Ed.), *Springer Handbook of Nanomaterials*, DOI 10.1007/978-3-642-20595-8_21,

ical reduction of metal ions [21.5, 6], hydrothermal synthesis method [21.7–11], ballistic deposition [21.12], powder metallurgy [21.13], filter casting [21.14], potential-controlled anodization [21.15, 16], electroplating [21.17], electrodeposition [21.18–20], potential-controlled displacement [21.21], surfactant emulsion template [21.22], catalytic chemical deposition method [21.23], one-step square-wave potential pulse treatment [21.24], inkjet printing–sintering technique [21.25], template-printing method [21.26], and wet-chemical strategy [21.27]. However, the dealloying strategy is at present the most popular method to prepare nanoporous metals with random porous structure. Dealloying refers to selective dissolution of one or more components out of an alloy. In fact, dealloying is an ancient process and has a long history. Indians of pre-Columbian Central America had invented such a technique (also named depletion gilding) for coloration of castings prepared from copper–gold alloys. A very closely related process for coloration of silver–gold alloys, known as cementation, is known to have been used by European and Near Eastern goldsmiths before the early Middle Ages [21.28]. At that time, however, people did not know about the formation of nanoporous structures during the dealloying or depletion gilding process.

Historically, dealloying has received significant attention in the context of corrosion, including stress corrosion cracking (SCC) and corrosion fatigue, such as dezincification of brass [21.29–40]; for example, dealloying was found to be a common feature of both intergranular and transgranular cracking during stress corrosion of Cu-Zn and Cu-Zn-Ni alloys [21.29]. Raney catalysts, named after their inventor Murray Raney, were well known throughout most of the last century [21.41]. They are formed by selective dissolution (usually by alkali) of an active metal (usually aluminum) from an alloy, leaving a noble metal residue which is an active hydrogenation catalyst [21.42]. Recently, dealloying has received renewed attention due to the fact that certain systems exhibit nanoporosity evolution upon dealloying. As early as the 1960s, *Pickering* and *Swann* [21.43, 44] used gold alloys as model systems to study their electrochemical behavior, and were also the first to use transmission electron microscopy (TEM) to characterize the resulting structures, which confirmed a nanoporous structure with feature size of ≈ 10 nm. In 1979, *Forty* [21.28] presented electron micrographs for a free-standing nanoporous gold (NPG) membrane material, which had pore size of approximately 20 nm and was made by etching an Ag-Au alloy film in HNO_3. Since the 1980s, *Sieradzki* and *Newman* and others have systematically investigated the corrosion process of Ag-Au alloys [21.45–47]. With advanced electrochemical techniques, such as electrochemical scanning tunneling microscopy, they discussed in great detail two key parameters associated with dealloying: the parting limit and the critical potential, where the parting limit defines the concentration of noble metal in an alloy above which dealloying does not occur, while the critical potential is empirically defined as a voltage threshold above which the dissolution current rises dramatically, resulting in substantial dealloying. At the very beginning of this century, *Erlebacher* et al. [21.48] further clarified the underlying physical mechanism of dealloying of Ag-Au alloys using experiments and computer simulation. After that, *Ding* and *Erlebacher* [21.49–52] continued to pay more attention to the microstructural morphology of NPG by dealloying commercial Ag-Au leaves. In the past 10 years, increasing interest has been paid to nanoporous metals made by dealloying, as well as their microstructures, unique properties, and potential applications.

21.1.1 Alloy Design of Precursors Suitable for Dealloying

Alloy systems that form porosity upon dealloying share a number of characteristics, and there are four basic common characteristics that an alloy typically possesses if it has a chance of becoming nanoporous during dealloying:

1. The difference in potential required to dissolve the alloy component in its pure form must be a few hundred millivolts, with one element being more noble (MN) and the other less noble (LN).
2. The composition is usually rich in the less noble component (the content of the more noble element is below its parting limit).
3. The alloy must be homogeneous with no phase separation prior to dissolution. Porosity evolution thus forms dynamically during dissolution and is not due to one phase simply being excavated from a two-phase material.
4. Diffusion of more noble atoms at the alloy/electrolyte interface must be sufficiently fast [21.53].

The prototypical alloy system for dealloying is Ag-Au, which has single-phase solid solubility across all compositions. Until now, dealloying has been observed in many binary alloy systems including Cu-based alloys (Cu-Au, Ag, Pt, Mn, Zr, Ni, etc.) [21.54–59],

Al-based alloys (Al-Au, Ag, Pt, Pd, Cu, etc.) [21.60,61], Mg-based alloys (Mg-Ag, Cu, etc.) [21.62, 63], Zn-based alloys (Zn-Pt, Au, Ag, Cu, etc.) [21.64–67], etc. These binary systems are composed of a single-phase solid solution, or a single-phase intermetallic compound or a combination of solid solution and/or intermetallic phase [21.68–70]. Accordingly, nanoporous metals such as Au, Ag, Pd, Pt, Cu, etc. can be fabricated through chemical or electrochemical dealloying of these binary precursors. Figure 21.1 shows typical scanning electron microscopy (SEM) micrographs of NPG obtained by dealloying Ag-Au leaf in nitric acid [21.51], and optical images before and after dealloying are also included.

Besides binary systems, dealloying can also be realized in ternary or multicomponent precursors [21.71, 72]. Dealloying of ternary or multicomponent precursors is more complicated than that of binary systems, but they also provide the opportunity to tune the microstructure of the as-obtained nanoporous metals and to fabricate nanoporous alloy materials. Other than crystalline precursors, some amorphous alloys (metallic glasses) can also be dealloyed to form corresponding nanoporous metals [21.73, 74]. In comparison with crystalline alloys, multicomponent metallic glasses are monolithic in phase with homogeneous composition and structure down to subnanoscale. In addition, the shapes of precursors are also diverse, and films, ribbons, powders, nanoparticles, nanowires, and even bulk form have been reported.

It is well established that the composition, structure, and phase constitution of precursors have a significant influence on the dealloying process and the formation of nanoporous metals. It has been reported that electrochemical dealloying of nanocrystalline 62Cu-38Zr films results in formation of porous copper with uniform diameter of approximately 500 nm. In contrast, no porous copper could be obtained from coarse-grained 62Cu-38Zr alloys under the same conditions [21.70]. The following routes are normally used to prepare precursors: melt casting, rapid solidification, rolling, surface alloying, template-assisted electrodeposition, vapor deposition, sputtering deposition, etc. It is obvious that one can control the dealloying process by adopting a proper processing method of precursors.

21.1.2 Formation Mechanisms of Nanoporous Metals by Dealloying

In 1967, *Pickering* and *Wagner* [21.75] argued that, when one metal is preferentially dissolved, it may be assumed that one or more of the following three mechanisms operate:

1. Both metals ionize followed by redeposition of the more noble metal.
2. Only the less noble metal ionizes and enters the solution, while the atoms of the more noble metal aggregate by surface diffusion.
3. Only the less noble metal ionizes and enters the solution, and atoms of both metals move in the solid phase by volume diffusion.

Later, *Forty* et al. [21.28, 76, 77] thought that the formation of the island–channel structure during dealloying of Ag-Au alloys can be explained in terms of a corrosion disordering/diffusion reordering model in which corrosion proceeds by selective dissolution of the less noble component, thereby creating a disordered surface layer which subsequently reorders by surface diffusion of gold adatoms. In 1989, *Sieradzki* et al. [21.78] developed a new model to account for all the known features of dealloying based upon percolation theory. Their Monte Carlo simulation results could reproduce many of the features usually associated with dealloying in real binary noble–metal alloy sys-

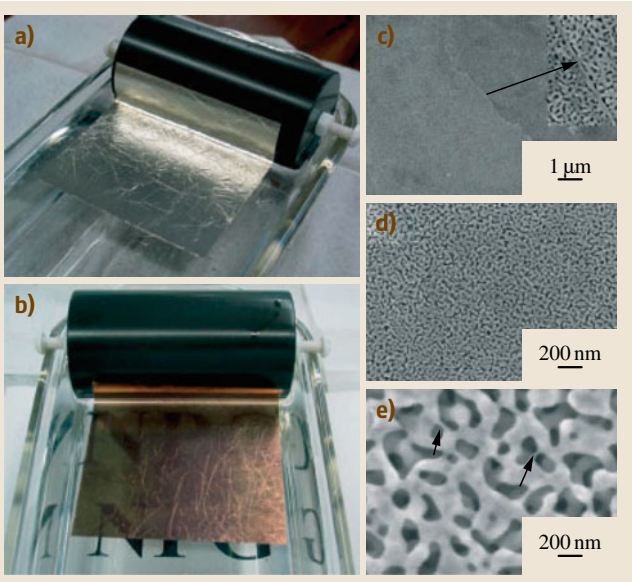

Fig. 21.1 (a–b) Optical and (c–e) SEM images of white gold leaf before and after dealloying in nitric acid for 15 min. The *inset image* in (c) shows a region where a slid grain boundary is located. Very thin gold ligaments with diameter smaller than 2 nm are often observed. Examples are marked with *arrows* in (e) (after [21.51])

tems, including the porous morphology of the dealloyed residue, coarsening of this porosity, sharp dealloying thresholds or parting limits, and the development of intermediate compositions.

In 2001, *Erlebacher* et al. [21.48] proposed a continuum model that is fully consistent with experiments and theoretical simulations of alloy dissolution, and demonstrated that nanoporosity in metals is due to an intrinsic dynamical pattern formation process; that is, pores form because the more noble atoms are chemically driven to aggregate into two-dimensional clusters by a phase separation process (spinodal decomposition) at the solid/electrolyte interface, and the surface area continuously increases owing to etching. Figure 21.2 clearly shows the simulated nanoporosity evolution during dealloying. Moreover, the nanoporous structure of NPG can be well modeled by their simulations. In 2004, *Erlebacher* [21.53] further described the microscopic details of porosity formation during dealloying as illuminated by a kinetic Monte Carlo model incorporating site coordination-dependent surface diffusion of all alloy components, and site coordination-dependent dissolution of the less noble atoms. Their simulation model can reproduce many of the characteristics of dealloying, particularly the observation of porosity evolution and reproduction of the classical phenomenology of a parting limit and a composition-dependent critical potential.

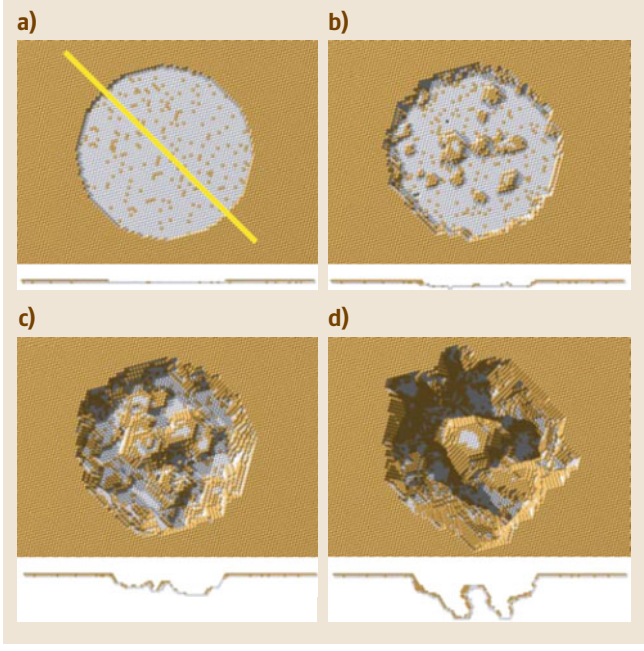

Fig. 21.2a–d Simulated evolution of an artificial pit in $Au_{10\%}$–$Ag_{90\%}$ (at.%), $f = 1.8$ eV. Cross-sections along the $(11\bar{1})$ plane defined by the *yellow line* in **(a)** are shown below each plan view. **(a)** The initial condition is a surface fully passivated with gold except within a circular region (the *artificial pit*). **(b)** After 1 s, the pit has penetrated a few monolayers into the bulk. We note how there are fewer gold clusters near the side wall than at the center of the pit. **(c)** After 10 s, a gold cluster has nucleated in the center of the pit. **(d)** At 100 s, the pit has split into multiple pits; each will continue to propagate into the bulk to form a porous structure (after [21.48])

Below the dealloying critical potential, passivation normally occurs, but its origin is still unclear. Recently, *Renner* et al. [21.79] revealed the microscopic structural changes associated with a general passivation phenomenon on the atomic scale by in situ x-ray diffraction with picometer-scale resolution. They observed the formation of a gold-enriched single-crystal layer that is two to three monolayers thick and has an unexpected inverted (CBA-) stacking sequence. At higher potentials, the protective passivation layer dewets and pure gold islands are formed; such structures form the templates for the growth of nanoporous metals.

It is known that, for most systems, the critical dealloying potential E_c is determined by a balance between dissolution-induced surface roughening and surface-diffusion-induced smoothing. Below the critical potential, the current density is surface diffusion limited and is typically less than $1\,\mu A/cm^2$. The conventional view of morphology evolution in the region below the critical potential is that the alloy surface maintains a stable planar interface while enriching in the more noble constituent. The current decay is believed to be correlated with the B (MN element) enrichment, but the current never drops identically to zero. *Wagner* et al. [21.80] studied in detail the dealloying behavior below the critical potential, and found the existence of different regimes of power-law current decay behavior at potentials below the critical potential. The initial current decay displays t^{-1} behavior, which their modeling has shown to be consistent with the exhaustion of sites available for dissolution. When the current from this process falls to a low enough level, the power law adopts an exponent indicative of one of three mechanisms dominating in the surface-vacancy diffusion process. The current resulting from the surface-diffusion-controlled process can follow $t^{-5/8}$, $t^{-1/2}$, and $t^{-1/4}$ behaviors, respectively, for surface-vacancy-controlled periphery diffusion, terrace diffusion, and evaporation–condensation.

It is well recognized that the formation of nanoporous metals by dealloying involves selective

dissolution of the less noble element coupled with coarsening of the more noble element by surface diffusion. However, minor dissolution of the more noble element is also possible during dealloying, especially when the electrolyte contains Cl^-. During dealloying of brass in aqueous sodium chloride, Cu dissolves into the solution to form Cu(I) and Cu(II) complex ions [21.31]. At appropriately high dealloying potentials, relatively steady chloride compound or chloride complexes can form between chloride ions and the more noble metals included, such as soluble $[AuCl_4]^-$, $PdCl_2$, $[AgCl_2]^-$, $[CuCl_2]^-$, and insoluble AgCl and CuCl during the electrochemical dealloying of Al-based alloys [21.61]. Eventually, the dissolution of Cu to form soluble $[CuCl_2]^-$ complex plays a key role in the dealloying of $MgCu_2$ and the formation of nanoporous copper [21.81]. Moreover, inductively coupled plasma (ICP) measurements also verify the existence of minor Ag ions in the electrolyte after chemical dealloying of Mg-Ag-Pd alloys [21.71]. In addition, the electrochemical dealloying mechanism of Al_2Au in neutral NaCl solution can be explained based upon the Pourbaix diagram and chloride ion effect [21.82]. During the dealloying process, a self-acidifying effect is triggered due to the dissolution and instant hydrolysis of Al^{3+}/Al, which is assisted by chloride ions in the electrolyte (Fig. 21.3). The self-acidifying effect accelerates the dealloying process of the Al-Au alloys and thus the formation of NPG.

If multiple phases exist in the alloy, *Pugh* et al. [21.55] argued that porosity formation of any individual phase would follow the same requirement for a single phase, and hence typically only the A-rich phase would dealloy (here A is the less noble element). In this case, dealloying would be isolated to only surface grains unless a mechanism existed for penetration of the electrolyte throughout the alloy; for example, the A-rich grains form a percolating path through the alloy. As for a two-phase alloy, we have found that the dealloying process depends upon the composition, activity, and electrochemical properties of each phase in the alloy. According to the reactions (being excavated, dealloyed, or retained) of the constitutive phases in a biphasic alloy during dealloying, six types of dealloying are classified, and four typical dealloying scenarios can be identified from the viewpoint of nanoporosity evolution during dealloying [21.61]. Moreover, it is interesting to note that dealloying of the less noble phase has a promoting effect on dealloying of the more noble phase (for example, Al-Ag alloys containing Al and Ag_2Al) [21.83]. In addition, the promoting effect in eutectic structures is stronger than that in peritectic structures, the effect of a solid solution as the less noble phase is stronger than that of an intermetallic phase, and the higher the diffusivity and the lower the equilibrium potential of the more noble element in the electrolyte, the more substantial the promoting effect is.

Most recently, the chemical dealloying mechanism of bimetallic Pt-Co nanoparticles (NPs) has been investigated on a fundamental level by the combination of x-ray absorption spectroscopy (XAS) and aberration-corrected scanning transmission electron microscopy (STEM) [21.84]. Structural parameters, such as coordination numbers, alloy extent, and the unfilled d states of Pt atoms, are derived from the XAS spectra, together with the compositional variation analyzed by line-scanning energy-dispersive x-ray spectroscopy (EDX) on an atomic scale, to gain new insights into the dealloying process of bimetallic Pt-Co NPs. The XAS results on acid-treated Pt-Co/C NPs reveal that the Co–Co bonding in the bimetallic NPs dissolves first, and the remaining morphology gradually transforms to a Pt skin structure. Furthermore, it is observed that such an imperfect Pt skin surface feature will collapse due to penetration of electrolyte into layers underneath and cause further dissolution of Co and the loss of Pt. The electrocatalytic activity decreases accordingly, if the dealloying process lasts for 4 h.

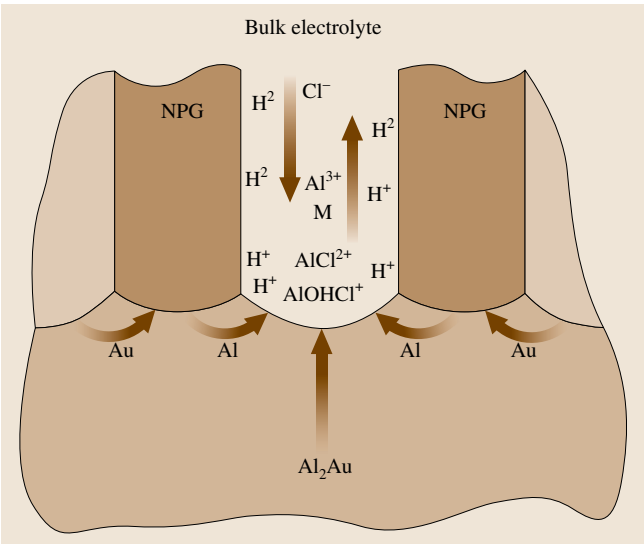

Fig. 21.3 Schematic illustration of pore evolution and hydrogen bubble emergence during electrochemical dealloying of Al_2Au in 10 wt % NaCl aqueous solution (after [21.82])

Normally, a minor residue of the less noble element is inevitable in the resultant nanoporous metals formed by dealloying, but less attention has been paid to the retention of the less noble element during dealloying. Recently, *Liu* et al. [21.85] investigated factors controlling retention of the less noble metal in nanoporous structures processed by electrochemical dealloying, taking Ag-Au as an example. It has been found that, while the dealloying critical potential is generally independent of pH, the dissolution rate is strongly affected by the solution acidity. pH substantially affects Ag retention in both the oxide and alloy forms. To discriminate between the retention forms, two different approaches employed for removing the Ag oxide from freshly dealloyed samples are: (i) oxide dissolution in 1 M $HClO_4$, and (ii) oxide reduction to elemental Ag followed by subsequent electrochemical oxidation to Ag^+ ions. Critical analysis of the experimental results suggests that the pH and dissolution rate affect more significantly the amount of Ag retained in the form of oxide, while the dealloying potential has a stronger impact on Ag trapping. In addition, the Ag retained as oxide is determined to be predominantly AgO. Their findings could enable the development of strategies for structural and compositional control in electrochemically processed metallic nanoporous materials.

21.1.3 Control over Structures of Nanoporous Metals

It is known that the properties of nanoporous metals are closely related to their microstructure and especially the characteristic length scale of ligaments/channels. It is of great importance to control the microstructures of nanoporous metals. Some factors including the microstructure of precursors, the kind and type of electrolytes, the applied dealloying potential, and the dealloying temperature and time will affect the dealloying process and thus the formation/structure of nanoporous metals. At the same time, formation of nanoporous metals by dealloying is a self-organization process by surface diffusion of the more noble element along the alloy/solution interface, and the surface diffusivity of the more noble element has a significant influence on the length scale of the ligaments/channels of nanoporous metals. We can tune the microstructure of nanoporous metals by adjusting the dealloying parameters, especially by control of the surface diffusivity of the more noble element.

Pt has a value of surface diffusivity ($< 10^{-19}\,cm^2/s$) that is at least 3–4 orders of magnitude lower than that ($< 10^{-15}$–$10^{-16}\,cm^2/s$) of Au under their respective electrochemical environment. Therefore, nanoporous Pt normally shows a ligament–channel structure with a length scale of only a few nanometers through dealloying of Cu-Pt and Al-Pt alloys [21.55, 60, 86]. Figure 21.4 shows TEM and high-resolution TEM (HRTEM) images of nanoporous Pt obtained by chemical dealloying of $Al_{88}Pt_{12}$ alloy in 20 wt % NaOH solution [21.60]. The corresponding selected-area electron diffraction (SAED) pattern and the HRTEM image confirm that the as-obtained nanoporous Pt is composed of randomly oriented face-centered cubic (fcc) nanocrystals. For a given dealloying solution, the length scale of the ligaments/channels in the resulting nanoporous metal is associated with surface diffusion of more noble atoms, and increases with increasing diffusion coefficients in the sequence: Pt/Pd < Au < Ag < Cu [21.60].

Antoniou et al. [21.87] reported synthesis of nanoporous platinum (np-Pt) through electrochemical dealloying in aqueous HF from cosputtered Pt_xSi_{1-x}

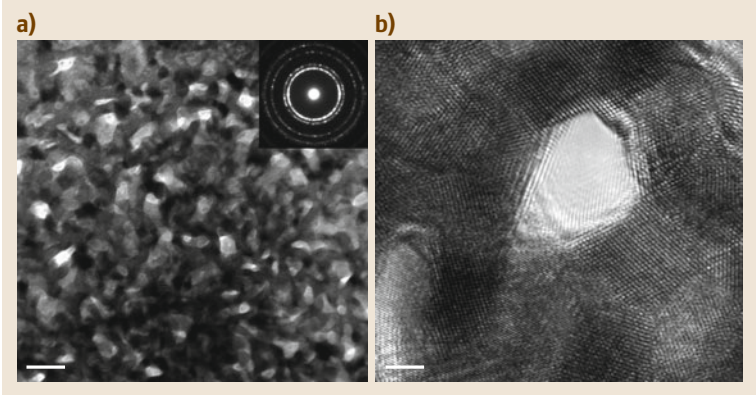

Fig. 21.4 **(a)** TEM image of nanoporous Pt obtained by chemical dealloying of $Al_{88}Pt_{12}$ alloy in 20 wt % NaOH solution. (*Inset*) Corresponding SAED pattern. *Scale bar*, 20 nm. **(b)** HRTEM image of nanoporous Pt. *Scale bar*, 2 nm (after [21.60])

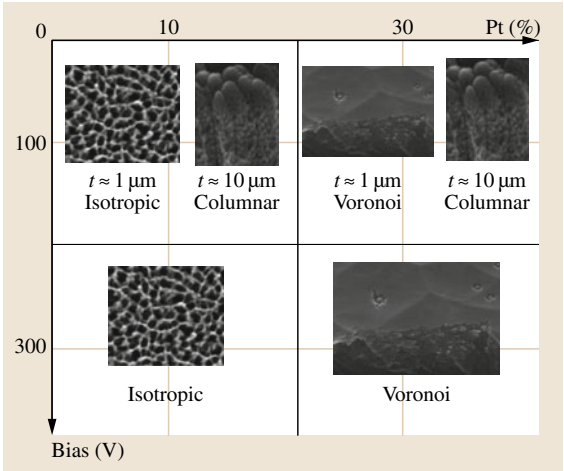

Fig. 21.5 Schematic of the possible np-Pt foam morphologies as a function of cosputtering parameters, initial alloy composition, and thickness (after [21.87])

amorphous films for different initial compositions and sputter bias conditions. They found that, in addition to the expected isotropic open-cell np-Pt foam, anisotropic columnar and Voronoi np-Pt is obtained. There are two levels of anisotropy: On the micron scale, 100 nm columns or 1 µm Voronoi polygons form, whereas inside the columnar and Voronoi hyperstructures, the ligaments and pores are anisotropic, ranging from 5 to 25 nm. The ligament diameter and grain size were 5 nm for all reported structures. A processing–structure map was developed to correlate np-Pt structure to the processing conditions (Fig. 21.5).

Monolithic nanoporous copper can be synthesized by dealloying $Mn_{0.7}Cu_{0.3}$ by two distinct methods: potentiostatically driven dealloying and free corrosion [21.57]. Both the ligament size and morphology were found to be highly dependent on the dealloying methods and conditions; for example, ligaments of 16 or 125 nm were obtained by dealloying either electrochemically or by free corrosion, respectively. Optimization of the starting Mn-Cu alloy microstructure allowed generation of uniform porous structures. *Seker* et al. [21.88] reported that thermal treatment of Ag-Au films can reduce microscale void formation in blanket nanoporous gold films. *Okman* et al. [21.89] found that the ramped potential increase gave better NPG film uniformity than stepped potential increase during potentiostatic dealloying of Ag-Au films. *Li* and *Balk* [21.90] reported effects of substrate curvature on dealloying of cosputtered Au-Pd-Ag alloy films. They found that ligament morphology, film cracking, and composition were significantly different for np-AuPd in concave versus convex film regions. Convex substrate curvature led to extensive film cracking, wide and high-aspect-ratio ligaments, and low residual Ag content. A more tensile stress state is believed to enhance the dissolution rate of Ag. *Li* et al. [21.91] reported that the microstructure of precursors has a significant influence on the dealloying of ternary amorphous Si-Pt-Ni precursors, and the ligament patterns and mechanical properties of the resulting nanoporous Pt-Ni alloys.

Snyder et al. [21.92] investigated dealloying behaviors of Ag-Au alloys in neutral silver nitrate solution. A small-pore (5 nm) NPG can be formed over a potential range of 1.3–2.0 V versus normal hydrogen electrode. They explained the observations in terms of residual surface oxides passivating the pores behind the dissolution front, which is itself acidified and thus corrosive due to accumulation of protons associated with oxide formation and water dissociation. Their method of fabricating NPG has the advantages of simplicity and safety. Linear relationships have been observed between the dealloying potential and the size of ligaments and pores [21.93]. Moreover, at low dealloying potential the pore size is larger than the ligament diameter, whereas at high dealloying potential they are comparable. *Li* and *Balk* [21.94] found that the pore and ligament dimensions of nanoporous palladium nickel (np-PdNi) were reduced by 50% when surfactants were added to the sulfuric acid etching solution. Ultrasonic agitation was also used to enhance dealloying and shortened the time required from 5 to 1 h, while retaining pore/ligament size of 5 nm.

During dealloying, adsorption of anions (such as Cl^-) from the electrolyte can accelerate surface diffusion of the more noble element. *Dursun* et al. [21.95] studied dealloying of $Ag_{0.7}Au_{0.3}$ and $Ag_{0.65}Au_{0.35}$ alloys in 0.1 M $HClO_4$ with addition of either 0.1 M KCl, 0.1 M KBr, or 0.1 M KI. They found that the critical overpotential decreases with addition of halides, with KI having the largest potential reduction of almost 50%. This decrease can be rationalized according to competition between the rates of increase of Au surface diffusivity and Ag exchange current density with halide addition. The size scale of porosity produced during dealloying of $Ag_{0.65}Au_{0.35}$ was found to increase with addition of halides. Also, it has been found that the length scale of ligaments/channels of nanoporous metals can be modulated by simply changing the dealloying solution (from HCl to NaOH) [21.60].

Low-temperature dealloying treatment is an effective method to tailor the characteristic length scale of

nanoporous gold. By systematically investigating the kinetics of nanopore formation during free corrosion, *Qian* and *Chen* [21.96] experimentally demonstrated that the dealloying process is controlled by diffusion of gold atoms at alloy/electrolyte interfaces, which strongly relies on the reaction temperatures. Low dealloying temperatures significantly reduce the interfacial diffusivity of gold atoms and result in ultrafine nanoporous structure. NPG with ultrafine ligaments/channels (less than 10 nm) can be obtained by dealloying of Al_2Au in alkaline solution at low temperature. The surface diffusivity of Au adatoms was evaluated as 2.1×10^{-23}, 2.3×10^{-21}, and $1.6\times10^{-19}\,m^2/s$ for dealloying at 253, 298, and 368 K, respectively. Measurement of the activation energy demonstrates that formation and coarsening of NPG are governed by Au diffusion at alloy/solution interfaces, regardless of the dealloying medium [21.97].

Addition of elements with low surface diffusivity into precursors can effectively refine the ligaments and channels of nanoporous metals (or alloys). In addition, as is well known, the noble metals Pt and Pd are widely used in the field of fuel cells as electrocatalysts and exhibit excellent catalytic activities for oxidation of small organic molecules. Introduction of Pt or/and Pd into nanoporous metals (such as NPG) can also generate a kind of novel bi-/trimetallic nanoporous functionalized alloys. Addition of Pt to precursor Ag/Au alloys was, upon dealloying, found to stabilize the morphology of the porous metal formed, to refine its pore size to nearly atomic dimensions, and to stabilize its morphology even in harsh chemical and thermal environments [21.99]. As Pt possesses much slower surface diffusion rates than Au, during dissolution, Pt embedded in exposed terraces should segregate to the edges of the growing vacancy island step edges,

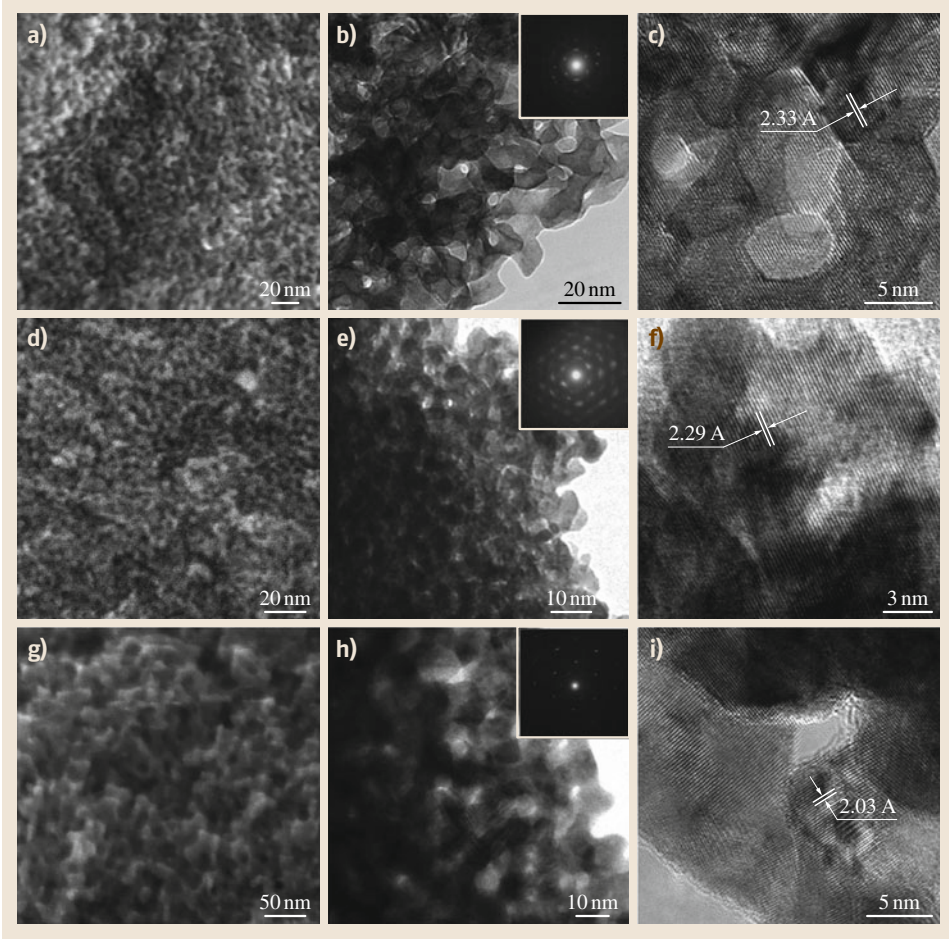

Fig. 21.6 SEM, TEM, and HRTEM images of nanoporous Au/Pt alloys obtained by dealloying **(a–c)** $Au_{10}Pt_{10}Cu_{80}$, **(d–f)** $Au_4Pt_{16}Cu_{80}$, and **(g–i)** $Au_{16}Pt_4Cu_{80}$ alloys, respectively (after [21.98])

stabilizing them and ultimately reducing the scale of porosity as well as leading to a Pt-rich shell. Selective etching of Cu from Au/Pt/Cu alloy precursors results in the formation of three-dimensional bicontinuous porous network structures with uniform pores and ligaments less than 10 nm (Fig. 21.6) [21.98]. Moreover, nanoporous Au/Pt alloys have a single-phase cubic structure with relatively uniform composition across the samples. The addition of the third element Pd into Mg-Ag results in the formation of an ultrafine nanoporous $Ag_{80}Pd_{20}$ alloy which exhibits superior catalytic activity towards electrooxidation of ethanol [21.71]. It has been found that elemental doping has no influence on the phase constitution of rapidly solidified Al-Au-Pt, Al-Au-Pd, and Al-Au-Pt-Pd alloys, and all these precursor alloys are composed of a single Al_2Au-type intermetallic compound (Al_2(Au,Pt), Al_2(Au,Pd), and Al_2(Au,Pt,Pd)). Ultrafine nanoporous gold alloys with ligaments/channels less than 10 nm can be facilely fabricated through dealloying these rapidly solidified Al_2Au-based precursors under free corrosion conditions. When performing dealloying in 20 wt % NaOH solution, a certain amount of Pt or/and Pd addition exhibits a superior refining effect, and the length scale of the ligaments/channels in the as-obtained np-Au alloys can reach $\approx$ 3 nm for Pt doping or Pt/Pd codoping. When performing dealloying in 5 wt % HCl solution, the anticoarsening capacity of Pt doping is more remarkable than that of Pd doping. In addition, the amount of doping can significantly affect the anticoarsening ability of ligaments/channels in thus-obtained np-Au alloys [21.72].

Generally, the structure of nanoporous metals can be coarsened to larger length scales (up to micrometers) at elevated temperatures and has been shown to coarsen at room temperature as a function of the applied voltage and electrolyte composition; for example, fast surface diffusion of gold in electrolyte gives NPG leaf the unique ability to have its porosity adjusted using simple room-temperature acid-induced postprocessing (Fig. 21.7) [21.51]. *Hakamada* and *Mabuchi* [21.100] reported a simple and spontaneous synthesis of a nanoporous gold prism microassembly with highly dense skins, which was achieved just by immersing nanoporous gold into concentrated hydrochloric acid. Coarsening of the porous structure can be attributed to the rapid surface diffusion of gold accelerated by Cl^-. Moreover, the morphology of the nanoporous gold prism microassembly was significantly different from that of annealed nanoporous gold.

Through combination with other routes such as template methods, galvanic replacement reactions, and underpotential deposition electroless plating, dealloying can be used to further tailor the morphology, microstructure, and properties of nanoporous metals. *Ji* and *Searson* [21.101] reported fabrication of nanoporous nanowires with high surface area and well-defined pore morphology (Fig. 21.8). The nanoporous nanowires were formed in a two-step process involving electrochemical deposition of a single-phase, two-component A_xB_{1-x} alloy into a nanoporous template (AAO), with subsequent chemical etching of one component from the alloy after removal from the template. Moreover, nonporous segments can be incorporated into

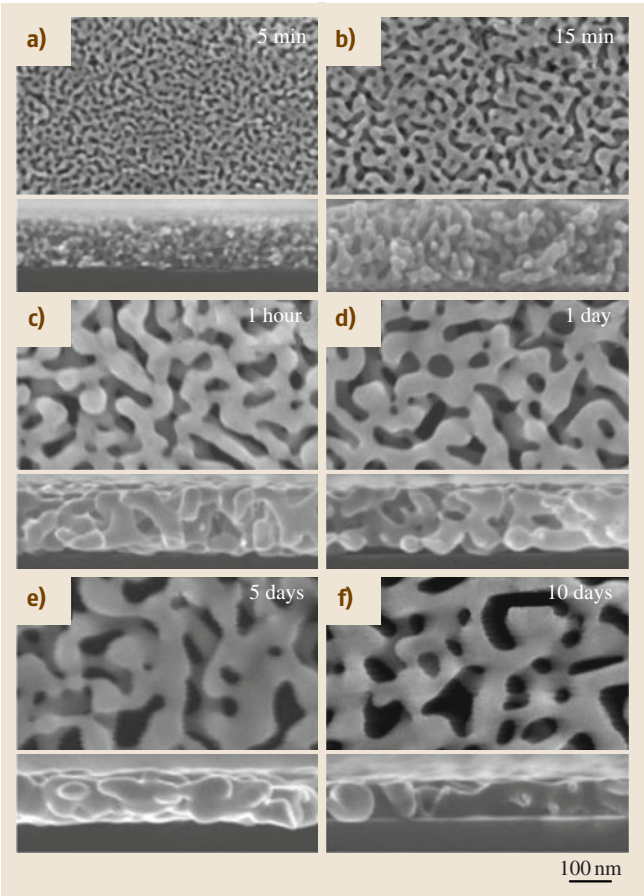

Fig. 21.7a–f Plan-view and cross-sectional SEM images of NPG leaf samples showing significant structure coarsening upon continued immersion in acid for extended times after the leaf is completely dealloyed (dealloying is usually complete after 5 min) (after [21.51])

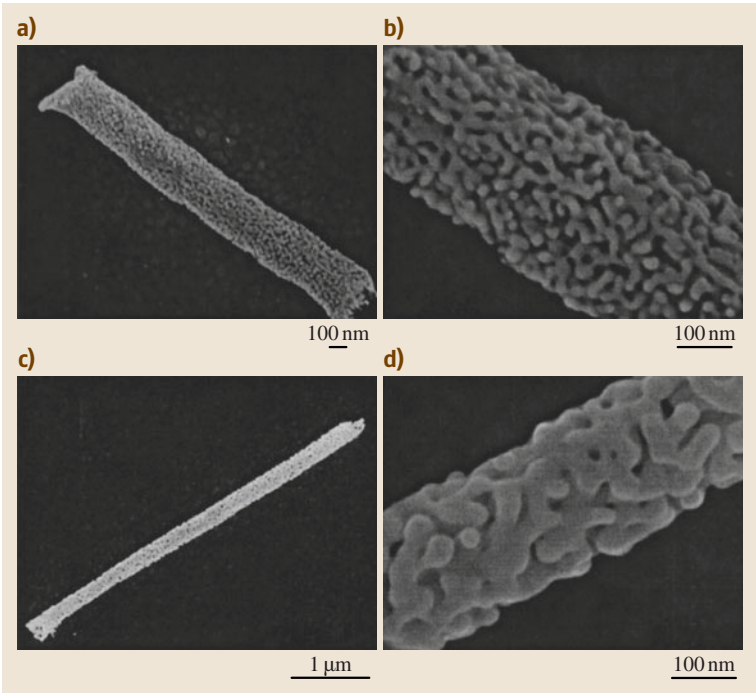

Fig. 21.8a–d SEM images of NPG nanowires (after [21.101])

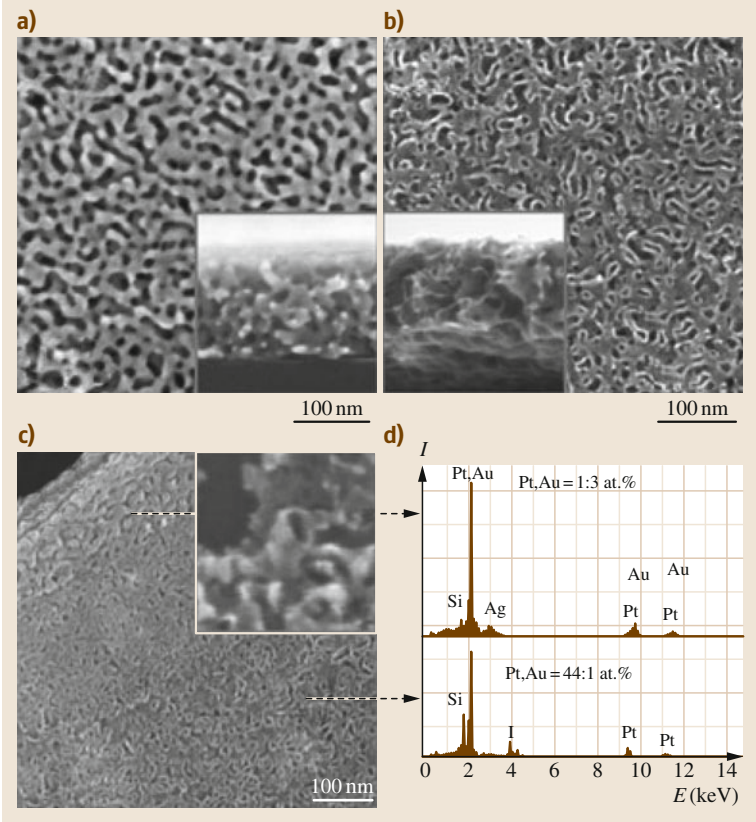

Fig. 21.9 **(a)** Plan-view and cross-section (*inset*) SEM images of NPG. **(b)** Plan-view and cross-section (*inset*) SEM images of NMP. **(c)** SEM image of a Pt-coated NPG sample within which gold has been only partially removed; the *inset* shows a tube opening of NMP. **(d)** EDS analysis indicates a gradual structure transition from Pt/NPG to NMP (after [21.52])

multisegment nanowires. *Chen* et al. [21.102] reported synthesis of a novel gold-decorated nanoporous copper (Au at NPC) core–shell composite. Thin gold shells with controllable thickness are homogeneously deposited onto the internal surfaces of three-dimensional (3-D) nanoporous copper via a spontaneous displacement reaction, while nanoporous copper is utilized as a reduction agent as well as 3-D template and substrate. *Ding* et al. reported the design and fabrication of nanotubular mesoporous platinum (NMP), a new material that can be described as a network of platinum nanotubes with diameter of about 15 nm and walls 1 nm thick that interconnect to form an open, doubly bicontinuous structure that may possess the highest surface-area to-volume ratio known for a macroscopic sample of metal (Fig. 21.9) [21.52]. Nanotubular mesoporous platinum can be synthesized by epitaxial casting using nanoporous gold membrane molds (dealloying–plating–dealloying). They further investigated the structure evolution of a novel electrocatalyst, Pt-decorated nanoporous gold (Pt-NPG), during thermal annealing at relatively low temperatures [21.103]. Pt-NPG was made by plating a thin layer of Pt over NPG substrate during an electroless plating process that generated epitaxial Pt nanoislands loaded on the NPG surface. In comparison with Pt's very high melting point, thermal annealing at temperatures as low as 100 °C was found to significantly change the structure and surface chemistry of these nanomaterials. While Pt-NPG preserved very well its initial porous morphology, the deposited Pt islands collapsed to form a thin Au-Pt alloy layer coating on the NPG surface upon heating. This structure change results in severe modulation of the electronic structure and surface reactivity of Pt, as proved by the markedly different behaviors in electrocatalytic reactions such as formic acid electrooxidation and CO stripping.

21.2 Properties of Nanoporous Metals

The phase constitution, microstructure, and composition of nanoporous metals can be characterized using XRD, SEM, TEM, HRTEM, x-ray photoelectron spectroscopy (XPS), energy-dispersive x-ray (EDX) analysis, atomic force microscopy (AFM), scanning tunneling microscopy (STM), small-angle neutron scattering (SANS), x-ray absorption spectroscopy (XAS), high-angle annular dark-field scanning transmission electron microscopy (HAADF-STEM), and many other techniques.

21.2.1 Structure and Morphology

Characterization Methods

Corcoran [21.104] explored the use of small-angle neutron scattering and scanning tunneling microscopy as potential tools for determining the mechanisms involved in porosity formation. The average pore size and distribution were found to depend upon the electrolyte composition, dealloying rate, applied potential, and time. Figure 21.10 shows in situ scattering data for spontaneous corrosion of $Ag_{0.7}Au_{0.3}$ in concentrated HNO_3. The length scale of nanopores can be evaluated from the characteristic peak position. *Fujita* and *Chen* [21.105] proposed a method derived from the fast Fourier transform (FFT) process to measure the characteristic length scale of bicontinuous nanoporous structures. By rotationally averaging the FFT power spectrum of a nanoporous micrograph from SEM or TEM, a significant peak in the power spectrum can be obtained, which reflects the characteristic length scale

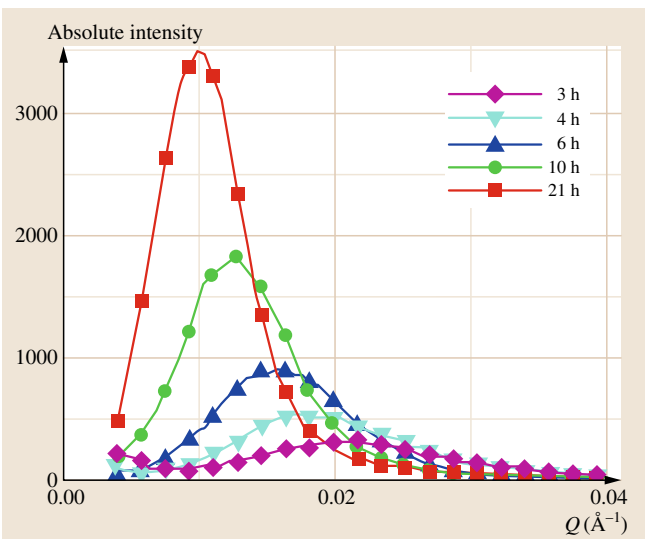

Fig. 21.10 In situ scattering data for spontaneous corrosion of $Ag_{0.7}Au_{0.3}$ in concentrated HNO_3. The *dealloying time* associated with each curve is indicated (after [21.104])

of the quasiperiodic structure. This method is valid for the bicontinuous morphology that is frequently observed in nanoporous metals prepared by chemical or electrochemical dealloying.

Renner et al. [21.107] presented an in situ x-ray diffraction study of the initial steps of potential-controlled, selective dissolution of Cu from a Cu_3Au (111) single-crystal surface immersed in 0.1 M H_2SO_4. They found structural evolution of an ultrathin Au-rich metallic passivation layer at low overpotentials toward thicker, pure Au islands at elevated overpotentials below the critical potential. The thickness of the ultrathin layer grows from two hexagonal close-packed (hcp) monolayers to several fcc-stacked monolayers. The epitaxial Au-rich layer, which exhibits a reversed stacking with regard to the single-crystal substrate, passivates the Cu_3Au (111) surface. Complementary ex situ AFM images showed at elevated overpotentials a surface completely covered with islands of a homogeneous size distribution, which agrees well with the findings from the x-ray experiments. The Au islands are found to be weakly hexagonally correlated.

Rösner et al. [21.108] developed a method to reconstruct a nanoporous metal (taking NPG as an example) in three dimensions from TEM images. Normally, the small feature sizes of NPG prevent characterization using many established techniques such as optical microscopy serial sectioning or x-ray tomography. The most important observations obtained using TEM tomography are:

1. The structure represents a contiguous network of branched ligaments.
2. The structure is quite inhomogeneous, with a broad distribution of ligament and pore diameters and shapes.
3. As a consequence, the specific surface area is larger than what would be estimated based on the characteristic ligament size.
4. In spite of the many saddle-point-like features, the average mean curvature is positive and close to what would be expected for convex objects of a size corresponding to the ligament diameter.
5. Encased voids are observed within the ligaments; there is no obvious explanation for the formation of these features.

This information contributes to establishing a basic description of the topology and local structure of nanoporous metals prepared by dealloying, which may form the basis for future models leading to predictive understanding of their properties, such as strength, surface induced strain, or transport properties.

Fujita et al. [21.106] reported transmission electron tomography of nanoporous gold fabricated by chemically dealloying $Au_{35}Ag_{65}$ films. A number of algorithms were employed to quantitatively characterize the complex three-dimensional nanoporous structure. It was found that gold ligaments and nanopore channels are topologically and morphologically equivalent; i. e., they are inverses of each other in three-dimensional space. Statistical analysis reveals that this bicontinuous nanostructured material is actually quasiperiodic and has, on average, near-zero surface curvature. Figure 21.11 shows corresponding 3-D tomographic reconstruction of nanoporous gold. These quantitative measurements will help in understanding the structural stability of nanoporous gold and in modeling its physical and chemical performance.

Petegem et al. [21.109] studied the evolution of the grain structure, internal strain, and lattice misori-

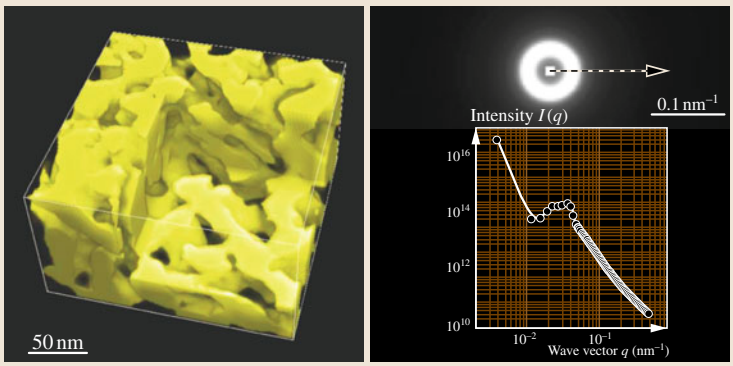

Fig. 21.11a,b 3-D tomographic reconstruction of nanoporous gold. **(a)** Magnified 3-D image revealing the internal bicontinuous structure of nanoporous gold. **(b)** Fourier-transformed pattern showing the quasiperiodic feature of nanoporous gold. The *inserted intensity profile* was taken along the *dashed arrow* in the Fourier-transform pattern (after [21.106])

entation of nanoporous gold during dealloying of bulk (3-D) Ag-Au alloy samples by various in situ and ex situ x-ray diffraction techniques including powder and Laue diffraction (Fig. 21.12a). Their experiments revealed that the dealloying process preserves the original crystallographic structure but leads to a small spread in orientations within individual grains. Initially, most grains develop in-plane tensile stresses, which are partly released during further dealloying. Simultaneously, the feature size of the developing nanoporous structure increases with increasing dealloying time. Finally, microdiffraction experiments on dealloyed micron-sized nanoporous pillars revealed significant surface damage introduced by focused ion beam milling. Figure 21.12b shows a two-dimensional (2-D) x-ray microdiffraction image of a nanoporous gold pillar. The inset displays a 3-D image of a part of the (111) ring.

Thin films of nanoporous gold, with ligaments and pores of the order of 10-nm diameter, offer a highly constrained geometry for deformation and thus provide an opportunity to study the role of defects such as dislocations in the plasticity of nanomaterials. *Sun* et al. [21.110] studied the mechanical behavior of nanoporous gold by using in situ nanoindentation in a transmission electron microscope. They found that dislocations were generated and moved along ligament axes, after which they interacted with other dislocations at the nodes of the porous network. For thicker films, the load–displacement curves exhibited load drops at regular intervals. Additionally, they also investigated the effect of the indenter displacement rate on the mechanical response of these gold films with nanoscale porosity. There appears to be a kinetic factor related to dislocation nucleation, where slower displacement rates cause load drops to occur at shorter distance intervals and over longer time intervals.

Liu et al. [21.111] developed an inexpensive, fast, selective, and sensitive technique for surface area measurement of metallic nanoporous materials (MNPM). Their approach is based on underpotential deposition (UPD) of metals on foreign substrates. In their work, Pb UPD on Au was chosen to illustrate the applicability, and revealed the advantages and limitations, of the proposed method. They measured the surface area of NPG electrodes with pore sizes in the range of 5–15 nm, prepared by electrochemical dealloying of single-phase AuAg. A critical comparison with Brunauer–Emmett–Teller (BET) analysis reveals important advantages of the method developed for surface area measurement in MNPM specimens.

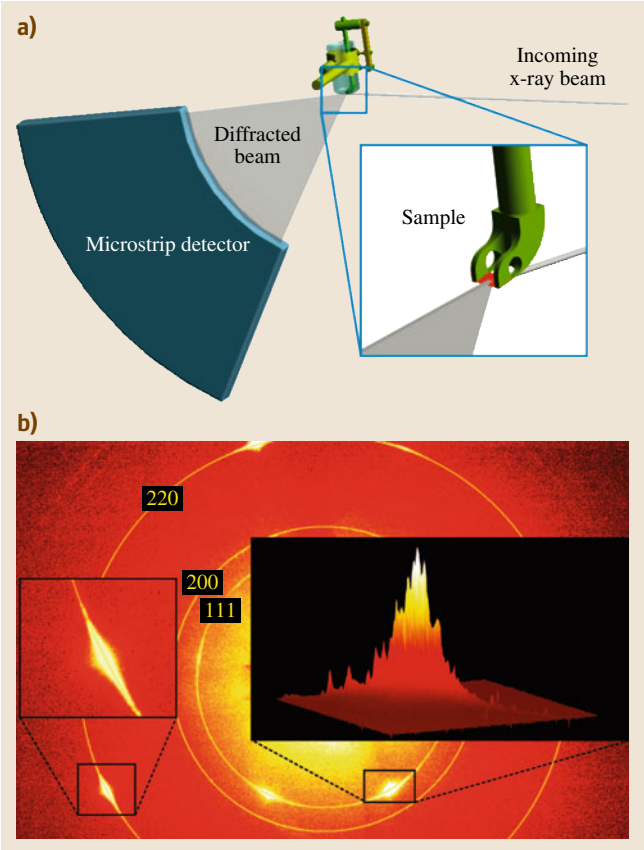

Fig. 21.12 **(a)** Schematic view of the in situ setup. **(b)** 2-D x-ray microdiffraction image of a nanoporous gold pillar. The *inset* displays a 3-D image of a part of the (111) ring (after [21.109])

Microstructure and Morphology

Through design of precursors and control over the dealloying process, nanoporous metals with diverse structures and morphologies can be fabricated, such as homogeneous structure, bimodal pore distribution, composite structure, ultrafine porous structure, etc. Moreover, both nanostructures (nanowires, nanotubes) and monolithic forms (films, ribbons, bulk samples) can be obtained. In addition, as well as pure metals, nanoporous alloys can also be produced.

Normally, larger-sized pores (hundreds of nm) are useful in microfluidic flow control, whereas very small pores (tens of nm) are useful for increasing device surface area as required for sensor applications. For microfluidic-based sensors, a bimodal pore size distribution composed of large porosity channels with highly porous channel walls is desirable to

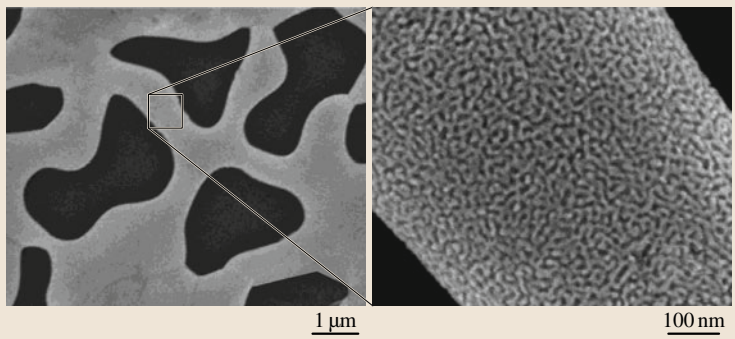

Fig. 21.13a,b A 2-D/3-D hybrid NPG structure, where the dimension of the unit structure in 2-D (1–2 μm) is two orders of magnitude larger than that in 3-D substructure (≈ 8 nm). Here, 100 nm-thick gold leaf was used, and the second-stage annealing was carried out at 500 °C for 8 h (after [21.49])

achieve fast response time and high sensitivity. *Ding* and *Erlebacher* [21.49] reported a two-step dealloying (dealloying–plating–annealing–dealloying) strategy to create nanoporous gold with multimodal pore size distributions. Figure 21.13 shows a 2-D/3-D hybrid NPG structure. In addition, NPG ribbons with bimodal channel size distributions can also be fabricated by chemical dealloying of Al-Au alloys composed of Al and Al_2Au phases [21.68]. The as-obtained NPG ribbons are composed of large-sized channels (hundreds of nanometers) with highly porous channel walls (tens of nanometers). Both large- and small-sized channels are 3-D, open, and bicontinuous. Moreover, the length scales of the large-sized channels can be modulated by changing the alloy composition, while those of the small ligaments/channels in the channel walls can be tuned by changing the dealloying solution.

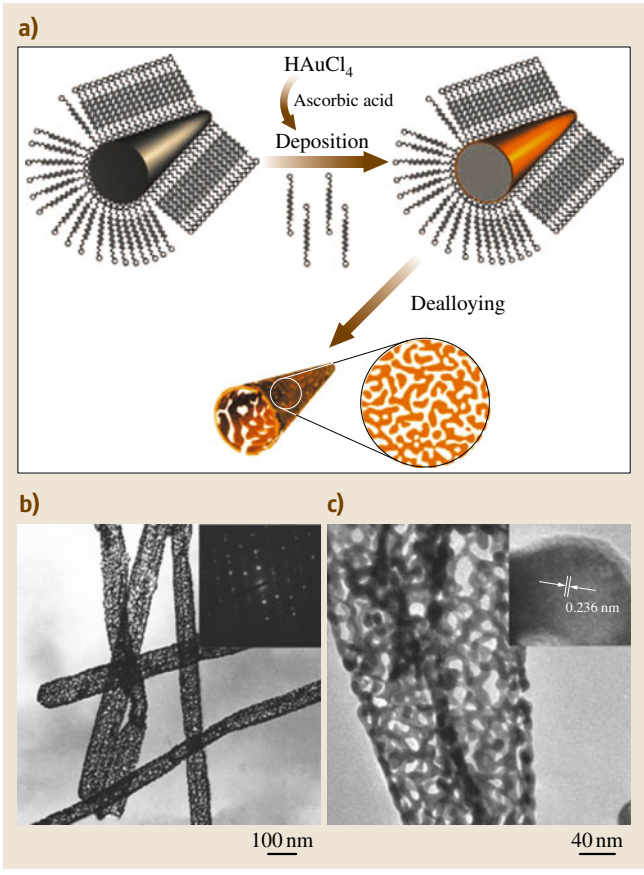

Fig. 21.14 (**a**) Schematic illustration of the synthesis process of Au-Ag alloy NPNTs. (**b–c**) TEM images of Au-Ag alloy NPNTs (after [21.112])

Yoo and *Park* [21.113] reported that ultrathin, platinum-coated, nanoporous nanorod arrays can be synthesized by electrodepositing gold and silver ions into porous alumina membranes, followed by selective dealloying and copper-UPD redox exchange reactions. Using a similar strategy, *Shin* et al. [21.114] synthesized hollow nanotubes (pore $d > 100$ nm) with nanoporous walls (pore $d < 10$ nm).

Metallic nanostructures with hollow interiors or tailored porosity represent a special class of attractive materials with intriguing chemicophysical properties. *Gu* et al. [21.112] recently reported the fabrication of a new type of metallic nanoporous nanotube structure based on a facile and effective combination of nanocrystal growth and surface modification. By controlling the individual steps involved in this process, such as nanowire growth, surface modification, thermal diffusion, and dealloying, one-dimensional (1-D) Ag-Au alloy nanoporous nanotubes (NPNTs) could be prepared with tailored structural features and predesigned functionalities. Figure 21.14a schematically shows the

synthesis process of Au-Ag alloy NPNTs, and the corresponding microstructures are presented in Fig. 21.14b,c.

We have found that high-surface-area Ag nanostructures can be used as novel effective template materials for construction of nanotubular mesoporous Pt/Ag and Pd/Ag alloy structures (Fig. 21.15), which are realized via room-temperature galvanic replacement reactions with H_2PtCl_6 and K_2PdCl_4 solutions by adding a high concentration of Cl^- ions as a coordinating agent [21.115]. Moreover, electrochemical measurements indicate that the resulting hollow and porous bimetallic nanostructures show enhanced electrocatalytic activities and CO tolerance with better durability toward methanol and formic acid oxidation due to alloying with Ag.

Due to the difference in dealloying between individual phases, a two-phase alloy can be dealloyed to form nanoporous metal composites. Nanoporous gold composites (NPGCs) can be produced through chemical dealloying of two-phase Al-Au alloys comprising Al_2Au and AlAu intermetallic compounds under free corrosion conditions [21.69]. The dealloying of Al_2Au and AlAu proceeds separately, resulting in the formation of the NPGCs. The microstructures of the NPGCs are composed of intracellular and intercellular areas which exhibit two kinds of nanoporous structures with different length scales of ligaments/channels. The nanoporous structure of the intracellular areas forms due to the dealloying of Al_2Au, while that of the intercellular areas forms owing to the dealloying of AlAu. Moreover, the proportion of the intercellular areas in the NPGCs increases with increasing Au content in the starting Al-Au alloys. Nanoporous palladium composites with second-phase embeddings can be fabricated through chemical dealloying of a rapidly solidified $Al_{70}Pd_{30}$ alloy in alkaline or acidic solutions under free corrosion conditions [21.116]. The experimental results show that the precursor alloy is composed of Al_3Pd and Al_3Pd_2 intermetallic compounds, and the resultant composites comprise the nanoporous palladium matrix dealloyed from Al_3Pd and the undealloyed Al_3Pd_2 embeddings.

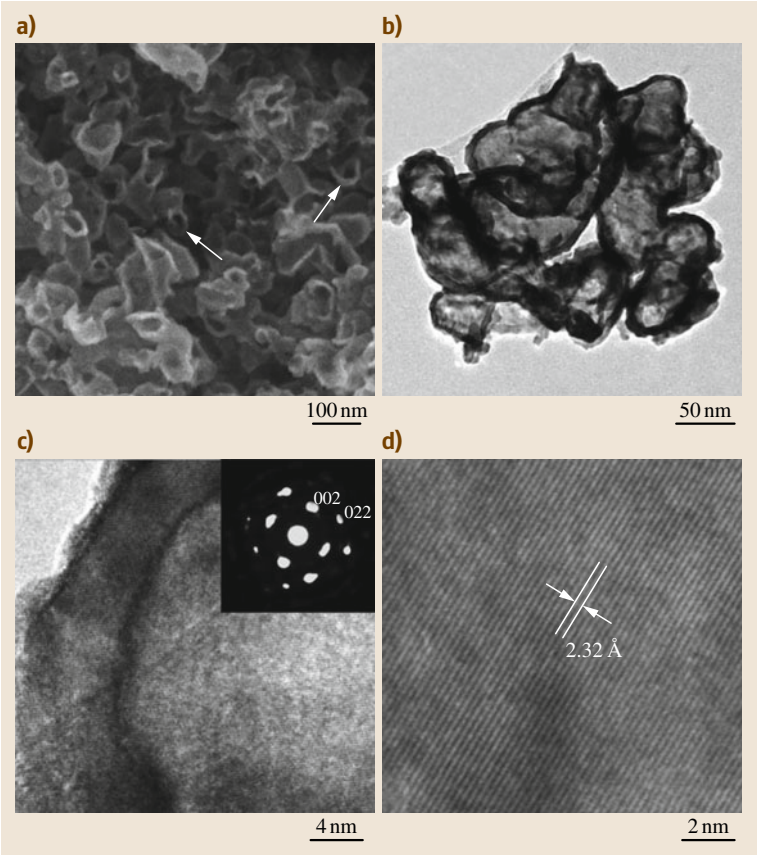

Fig. 21.15 **(a)** SEM, **(b–c)** TEM, and **(d)** HRTEM images of the sample resulting from reacting nanoporous silver (NPS) with $[PtCl_6]^{-2}$ solution. The *inset* in **(c)** is the corresponding SAED pattern (after [21.115])

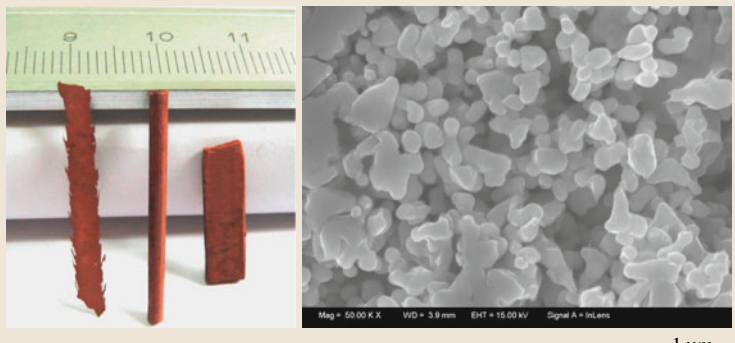

Fig. 21.16 (a) Macrograph showing nanoporous Cu ribbon, rod, and slice obtained by two-step dealloying of Al-40 at % Cu (*from left to right*). (b) SEM image of nanoporous Cu rod (after [21.117])

In addition, bulk nanoporous Cu ribbons, rods, and slices (of centimeter scale) can be fabricated by dealloying of Al-Cu alloys under free corrosion conditions (Fig. 21.16) [21.117]. These nanoporous Cu ribbons and bulk rods/slices can serve as model materials to investigate the mechanical, physical (for example, electrical resistivity), and chemical properties associated with the random porous structure of nanoporous solids.

21.2.2 Catalytic Properties

Due to their very high specific surface area and nanosized ligaments, nanoporous metals show excellent catalytic properties for a series of important heterogeneous reactions.

Despite the general inertness of gold, finely dispersed gold nanoparticles on suitable oxide supports can demonstrate remarkable catalytic activity for propene epoxidation or CO oxidation. Gold-based catalysts have potential applications in automotive emission control, because unlike platinum or palladium catalysts, they remain active at low temperatures (room temperature). *Zielasek* et al. [21.119] first pointed out that nanoporous gold is a promising material for catalytic applications, because it is self-supporting, thermally and mechanically stable, and shapeable; as a thin foil it could possibly find use as a membrane catalyst. Almost at the same time, *Xu* et al. reported that unsupported nanoporous gold could show extraordinary properties in low-temperature CO oxidation (−30 °C) [21.118]. Figure 21.17 shows the catalytic performance of a-NPG at different temperatures. It was believed that the curved shape of the ligaments could accommodate a high density of low-coordinated surface sites, such as step and kink atoms, which are responsible for the observed catalytic activity. More detailed studies have been carried out on this new catalytic system, including discussion of the active sites of catalysts, the reaction kinetics, and the dependence of the activity on space velocity and temperature [21.120]. The results show strong evidence that metallic gold atoms on NPG are the intrinsic active sites at which the reaction of CO with O_2 occurs. The kinetic study found that the reaction rate of CO oxidation on unsupported NPG depends significantly on the

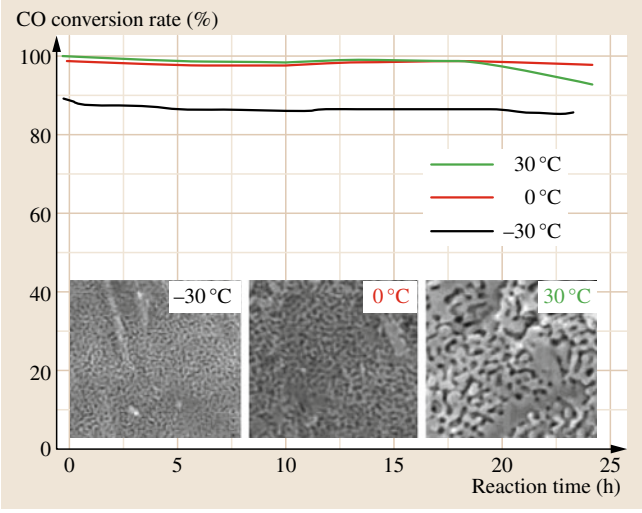

Fig. 21.17 Catalytic performance of a-NPG at different temperatures. In each experiment, 50 mg NPG catalyst and a gas mixture of 1% CO, 10% O_2, and 89% N_2 were used with flow rate of 66.7 ml/min, corresponding to space velocity of 80 040 ml/h gcat. The turnover frequency (TOF) was measured to be about 0.034 s^{-1}. *Insets* are SEM images of NPG samples after catalytic reactions. *Scale bars*: 100 nm (after [21.118]) ◀

CO concentration but only slightly on the O_2 concentration, suggesting that CO adsorption plays a decisive role in CO oxidation on NPG as the rate-limiting step.

Wittstock et al. [21.122] recently reported that nanoporous Au can catalyze selective oxidative coupling of methanol to methyl formate with selectivity above 97% and high turnover frequencies at temperatures below 80 °C. Because the overall catalytic characteristics of nanoporous Au are in agreement with studies on Au single crystals, they deduced that the selective surface chemistry of Au is unaltered but that O_2 can be readily activated with this material. Residual silver is shown to regulate the availability of reactive oxygen.

Recently, *Han* et al. found that nanoporous gold catalysts made by dealloying could be applied in gas-phase selective oxidation of benzyl alcohol to benzaldehyde, delivering good catalytic activity with high selectivity under ambient reaction conditions (Fig. 21.18) [21.121]. By increasing the concentration of oxygen in the gas mixture, the conversion increased greatly, accompanied by a slight decline in selectivity. By using pure oxygen, over 61% conversion with 95% selectivity was achieved at 240 °C. Interestingly, after the catalysts were pretreated with NaOH, the catalytic activity was promoted considerably. The dependence on residual Ag of the performance of NPG catalysts was tested, and in general, higher Ag content did not seem improve the activity and selectivity of NPG for benzyl alcohol oxidation. However, this study cannot rule out the possibility that low levels of Ag may contribute as a promoter to improve the selectivity.

As to the unsupported nature of NPG, however, there is still controversy. *Haruta* [21.123] classified the hypotheses for the active states of gold proposed so far as follows, in order of decreasing size of the gold catalyst:

1. Unsupported gold
2. Junction perimeter between gold and the metal-oxide supports
3. Specific size or thickness of gold clusters or thin layers
4. Cationic gold

He argued that gold nanoporous foams, the surfaces of which might be substantially contaminated by Ag_2O fine particles or patches, are highly active at temperatures even below 0 °C without water and OH^- ions. Actually, the catalysts can be regarded as inversely supported gold catalysts, and the junction perimeters between gold and Ag_2O can account for the high catalytic activity, as in the cases of TiO_2, Fe_2O_3, Co_3O_4, NiO, and CeO_2 supports (hypothesis 2). *Wittstock* et al. [21.124] investigated NPG with respect to its morphology, surface composition, and catalytic properties. In particular, they studied the reaction kinetics for low-temperature CO oxidation in detail, taking the mass transport limitation due to the porous structure of the material into account. Their results revealed that Ag, even if removed almost completely from the bulk, would segregate to the surface, resulting in surface concentrations of up to 10 at. %. While no Ag_2O was observed, they believed that Ag plays a significant role in activating molecular oxygen. Therefore, they thought that NPG should be more appropriately considered as an unsupported bimetallic catalyst rather than a pure Au catalyst.

Fig. 21.18 NPG shows high selectivity and conversion for gas-phase selective oxidation of benzyl alcohol to benzaldehyde (after [21.121])

Most recently, *Moskaleva* et al. [21.125] investigated the catalytic properties of nanoporous gold foams via CO and oxygen adsorption/coadsorption. They analyzed experimental results using theoretical models representing flat Au(111) and kinked Au(321) slabs with Ag impurities. Their results show that Ag atoms incorporated into gold surfaces can facilitate the adsorption and dissociation of molecular oxygen on them. CO adsorbed on top of six-fold-coordinated Au atoms can in turn be stabilized by coadsorbed atomic oxygen by up to 0.2 eV with respect to the clean, unsubstituted gold surface. These experiments suggest a link between the most strongly bound CO adsorption state and the catalytic activity of np-Au. Thus, they believed that their results shed light on the role of silver admixtures in the striking catalytic activity of unsupported gold nanostructures.

NPG catalysts made by dealloying Ag/Au alloys were found to be novel unsupported Au nanocatalysts that exhibited effective catalytic activity and high selectivity ($\approx$ 99%) for aerobic oxidation of D-glucose to D-gluconic acid under mild conditions [21.126]. The activity dependence as functions of pH value, temperature, NPG ligament size, reaction active sites, and reaction kinetics was discussed in great detail. The pos-

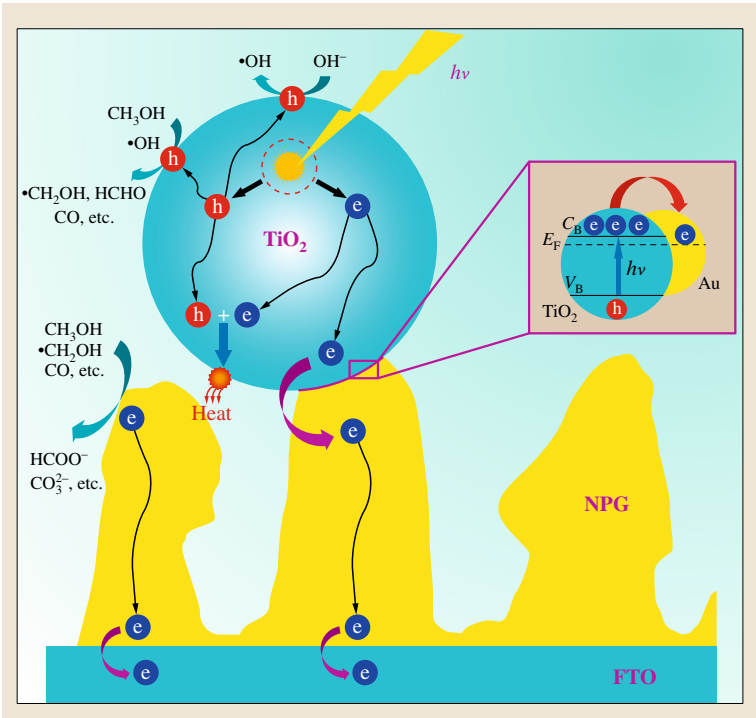

Fig. 21.19 Schematic illustration of a possible mechanism for methanol photoelectrocatalysis on the TiO_2/NPG electrode under UV illumination (after [21.127])

sible contribution from the residual Ag atoms trapped in the NPG ligaments was also discussed, which turned out to be unfavorable for glucose oxidation. The unexpected observation of catalytic activity of NPG with ligament size as large as 60 nm indicated that low-coordinated surface Au atoms should be the reaction active sites for glucose oxidation.

Recently, *Jia* et al. found that commercial TiO_2 nanoparticles can be assembled on the surface of NPG to fabricate novel TiO_2/NPG nanocomposite electrodes [21.127]. Large photocurrent and nearly reversible voltammetric responses were observed for methanol photoelectrocatalysis under ultraviolet (UV) radiation, indicating effective elimination of gold surface passivation due to a pronounced synergistic effect between TiO_2 and NPG. A possible mechanism was proposed to elucidate such a synergistic effect, based on the reaction of photogenerated reactive intermediates on the surface of NPG (Fig. 21.19). Kinetic studies showed that the coupling of TiO_2 with NPG in the system could lead to about a 30% decrease of apparent activation energy for methanol electrooxidation. In addition, porous AgCl/Ag nanocomposites show enhanced visible-light photocatalytic properties for degradation of methyl orange (MO) dye [21.128].

Asao et al. [21.129] recently discovered that nanoporous gold exhibited remarkable catalytic activity for oxidation of organosilane compounds with water. The catalyst was easily recoverable and could be used at least five times without leaching or loss of activity. The observed excellent durability of the catalyst was also confirmed by SEM images. Indeed, the nanoporous structure of the catalyst did not change, even after five uses for oxidation of dimethylphenylsilane.

21.2.3 Electrocatalytic Properties

Nanoporous metals represent a new class of high-surface-area nanostructures, where the interconnected interstices and channels extending in all three dimensions allow unblocked transport of medium molecules and electrons, which is particularly desirable for catalysis. In addition, made by dealloying in aqueous solutions, nanoporous metals have extremely clean surfaces, readily available for surface electrode reactions. Being support free and particle free, nanoporous metals completely eliminate the support corrosion problem and particle aggregation/sintering problem. It is thus interesting to explore their electrocatalytic performance by evaluating their potential in important energy con-

version applications, such as as anode catalysts in fuel cell technology.

NPG made by dealloying Au-Ag has been investigated as a novel electrode material for methanol electrooxidation [21.130]. Compared with bulk Au electrode, oxidation and subsequent reduction of NPG occur at significantly negative potentials in both acid and alkaline solutions. NPG shows great catalytic activity for methanol electrooxidation, but the structure quickly coarsens upon long-time potential cycling. Interestingly, after surface modification with only a tiny amount of platinum, NPG exhibits greatly enhanced electrocatalytic activity toward methanol oxidation in alkaline solution, which is exemplified by a broad and high anodic peak during the positive scan and two secondary oxidation peaks in the subsequent reverse scan. At the same time, SEM observation and long-time potential cycling both prove that Pt-NPG has greatly enhanced structure stability as compared with bare NPG. *Yu* et al. [21.131] also reported that self-supported nanoporous gold film electrodes show high catalytic activity and stability in direct electrooxidation of methanol.

Ge et al. investigated an ultralow-platinum-loading electrocatalyst based on a novel nanoporous membrane metal (NPG leaf), and its excellent performance toward methanol and CO electrooxidation [21.132]. Although it is widely accepted that the highest Pt utilization can be achieved only on monolayer (or submonolayer) type structures, to which these NPG-based nanostructures are close, the most important characteristic of Pt-NPG-type structures is the easy accessibility to almost all surface precious atoms by target molecules, which the current fabrication protocol based on physical mixing of nanoparticles can hardly achieve. This can explain why 0.5 min Pt-NPG samples exhibit much better performance than commercial Pt/C, although they have similar platinum utilization values. Considering the structure flexibility of NPG and the strong synergistic effect between Pt and Au, Pt-NPG may represent an alternative ultralow precious-metal loading catalyst to traditional ones with promising performance in important green energy technologies, such as direct methanol fuel cells (DMFC). Furthermore, by effectively enhancing the Pt utilization and providing a unique surface structure, electrooxidation of formic acid on Pt-NPG was found to be highly sensitive to its surface structure [21.133]. An unparalleled increase by nearly two orders of magnitude in catalytic activity was achieved on NPG electrodes decorated with submonolayer Pt atoms, as compared with commercial Pt/C catalyst under the same testing conditions. Figure 21.20 shows the catalytic activity of Pt-NPG membrane catalysts towards electrooxidation of small organic molecules. Through a simple immersion–electrodeposition (IE) method, a tiny amount of Pt can be deposited in quasi-two-dimensional form onto the NPG substrate, forming nanostructured bimetallic Pt-Au catalysts [21.134]. Such Pt-Au nanostructures have much higher structural stability than the bare NPG. Moreover, they exhibit better catalytic activity and stronger poison resistance than commercial Pt-Ru catalysts because of the synergistic effect of the bimetallic composition.

Ultrathin Pt films from one to several atomic layers can be decorated onto NPG membranes by utilizing UPD of Cu onto Au or Pt surfaces, followed by in situ redox replacement reaction (RRR) of UPD Cu by Pt [21.135]. The thickness of Pt layers can be controlled precisely by repeating the Cu-UPD-RRR cycles. TEM observations coupled with electrochemical testing suggest that the morphology of the Pt overlayers changes from an ultrathin epitaxial film in the case of one or two atomic layers to well-dispersed nanoislands in the case of four and more atomic layers. Moreover, the as-prepared NPG-Pt membranes maintain a single-crystalline structure, even though the thickness of the Pt films reaches six atomic layers, indicating that the decorated Pt films retain the same crystallographic relationship to the NPG substrate during the entire fabrication process. Due to the regular modulation of Pt utilization, the electrocatalytic activity of NPG-Pt exhibits interesting surface structure dependence in methanol, ethanol, and CO electrooxidation reactions (Fig. 21.21). These novel bimetallic nanocatalysts show excellent electrocatalytic activity and greatly enhanced poison tolerance as compared with commercial Pt/C catalysts.

Recently, *Wang* et al. successfully fabricated a new type of sandwich-type nanostructured electrocatalyst, NPG-Pt-Au, that simultaneously fulfills three key requirements as a good practical formic acid electrooxidation catalyst: ultralow Pt loading, great tolerance to poisoning, and high stability (Fig. 21.22) [21.136]. Time-resolved surface-enhanced infrared absorption (SEIRA) spectroscopy demonstrated that the greatly enhanced catalytic activity was achieved by changing the reaction pathways by using Au surface clusters, which also contribute to the stabilization of the catalyst. Considering that it is possible to tailor the respective structures and compositions within each structure unit, this work represents a general design strategy to

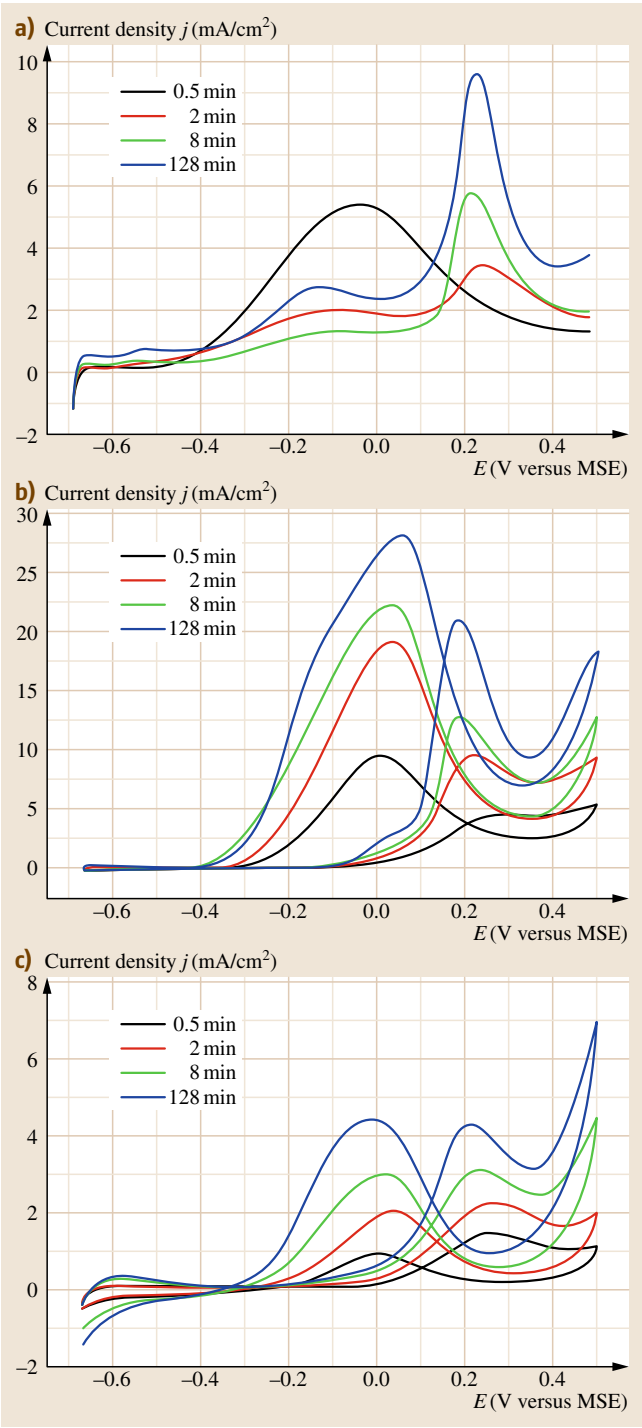

Fig. 21.20a–c Cyclic voltammetry (CV) curves for Pt-NPG samples in **(a)** 0.1 M $HClO_4$ + 0.1 M HCOOH, **(b)** 0.1 M $HClO_4$ + 0.1 M HCHO, and **(c)** 0.1 M $HClO_4$ + 0.1 M CH_3CH_2OH (MSE = mercury/mercurous sulfate electrode) (after [21.133]) ◀

functional nanocatalysts that shows great potential for various energy and environmental applications.

It is known that monometallic Pt is susceptible to deactivation or poisoning during catalytic and electrocatalytic processes; for example, Pt catalysts can be deactivated due to carbon deposition or coking in many heterogeneous catalytic reactions, and can also be poisoned by CO adsorption due to the strong bonding of CO on the Pt surface. Adding a second metallic component can enhance the activity, selectivity, and stability of pure metal catalysts. It has been reported that formation of bimetallic alloy nanostructures with other metals, such as Ru, Ag, and Au, can reduce CO poisoning. Nanoporous Au-Pt and Pt-Ru alloys with predetermined compositions can be fabricated through selective etching of Cu and Al from CuAuPt and PtRuAl precursors [21.98, 137]. Moreover, these high-surface-area alloy nanostructures show greatly enhanced specific activity and distinct surface reactivity toward electrooxidation of some small organic molecules, such as methanol and formic acid. The interaction between constituent metal elements may lead to special surface ensembles with unique structural properties, which can exhibit strong synergistic effects with greatly enhanced catalytic activities under appropriate conditions.

In addition, dealloying has been found to be an effective route to enhance the electrocatalytic properties of some other nanostructures, such as core–shell nanoparticles, nanowires, etc. *Shao* et al. [21.138] reported synthesis of a core–shell catalyst consisting of a Pt monolayer as the shell and porous/hollow Pd-Cu alloy nanoparticles as the core. The porous/hollow Pd-Cu nanoparticles were fabricated by selectively dissolving a less noble metal, Cu, using an electrochemical dealloying process. The Pt mass activity for the oxygen reduction reaction (ORR) of a Pt monolayer deposited on such a porous core is 3.5 times higher than that of a Pt monolayer deposited on bulk Pd nanoparticles and 14 times higher than that of state-of-the-art Pt/C electrocatalysts. *Strasser*'s group found that voltammetric dealloying of bimetallic platinum–copper (Pt-Cu) alloys is an effective strategy to modify the surface electrocatalytic reactivity of Pt bimetallic nanoparticles [21.139–

141]. The dealloyed active catalyst phase consists of a core–shell structure in which a multilayer Pt-rich shell surrounds a Pt-poor alloy particle core. The electrocatalytic Pt mass activity of the dealloyed core–shell particles for the ORR exceeds that of state-of-the-art Pt electrocatalyst by more than a factor of 4 and thus meets performance targets for fuel cell cathodes [21.142]. *Liu* et al. [21.143–145] fabricated nanoporous Pt-Co, Pt-Ni, and Pt-based multimetallic alloy nanowires through the combination of electrodeposition into AAO templates with dealloying. These nanoporous alloy nanowires exhibit distinctly enhanced electrocatalytic activities toward methanol oxidation as compared with current state-of-the-art Pt/C and PtCo/C catalysts.

The improvement of catalysts for the four-electron ORR ($O_2 + 4H^+ + 4e^- \rightarrow 2H_2O$) remains a critical challenge for fuel cells and other electrochemical energy technologies. Recently, *Snyder* et al. [21.146] showed that a tailored geometric and chemical materials architecture can further improve ORR catalysis by demonstrating that a composite nanoporous Ni-Pt alloy impregnated with a hydrophobic, high-oxygen-solubility, protic ionic liquid has extremely high mass activity (Fig. 21.23). They stated that the results are consistent with an engineered chemical bias within a catalytically active nanoporous framework that pushes the ORR towards completion.

21.2.4 Mechanical Properties

Mechanical breakdown or fracture in random porous media has been the subject of considerable computational and theoretical research [21.147]. Nanoporous metals should serve as a new model system for studying various physical properties and mechanical properties associated with three-dimensional random porous structures.

It should be noted that in network systems the terms "ductile" and "brittle" refer to the nature of the damage introduced into the sample during the fracture process. If many separated or distributed microcracks develop in the sample during fracture, the behavior of the system is termed *ductile*, and if only a few cracks form in the sample prior to failure, it is characterized as *brittle*. *Li* and *Sieradzki* [21.148] first observed a microstructural length scale-controlled ductile–brittle transition in NPG, similar to previous results for a network system described by *Kahng* et al. [21.149]. The sample-size-driven ductile–brittle transition may be quite universal with respect to the exact nature of the constitutive behavior of the individual ligaments in the random

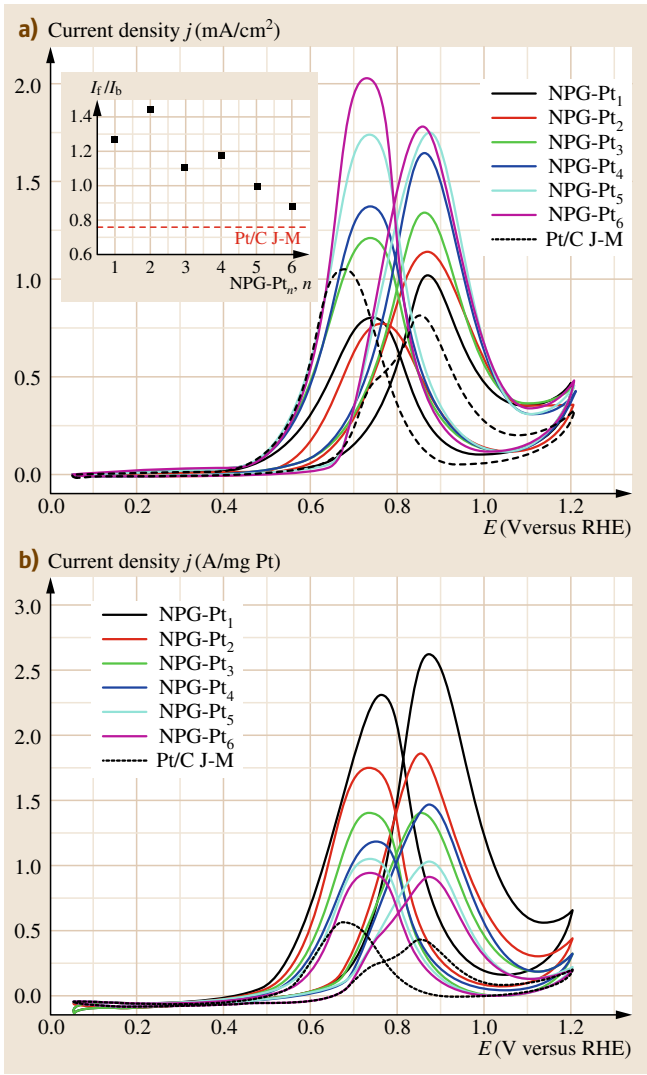

Fig. 21.21a,b ECSA (**a**) and mass (**b**) normalized CVs of NPG-Pt_n for methanol electrooxidation in 0.5 M H_2SO_4 + 1.0 M CH_3OH. CV curve (*dotted black line*) for a commercial Pt/C catalyst (Johnson Matthey, 20 wt %) is also included for comparison. The *inset* in part (**a**) shows the I_f/I_b values of NPG-Pt_n along with that for the commercial Pt/C catalyst (*red line*). Scan rate: 20 mV/s (RHE = reversible hydrogen electrode) (after [21.135])

structure. Thus, the strong length scale dependence of the mechanical behavior of NPG makes it a particularly useful material to study nanoscale mechanics.

The question still remains whether the brittle nature of nanoporous Au is caused by intrinsic brittleness of Au ligaments on the nanometer length scale or is

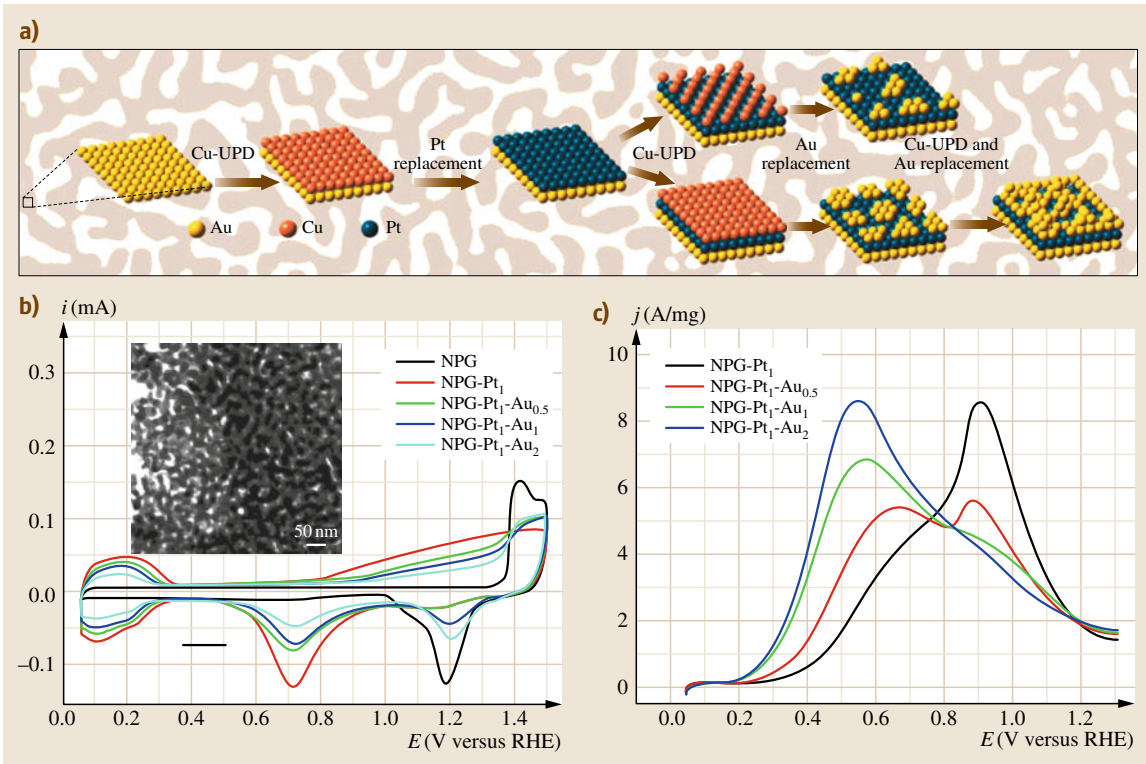

Fig. 21.22 **(a)** Schematic illustration of the fabrication procedure of NPG-Pt_1-Au_x catalysts. **(b)** Electrochemical CV for NPG-Pt_1-Au_x catalysts in 0.5 M H_2SO_4 (RHE, reversible hydrogen electrode). *Inset*: TEM image of NPG. **(c)** Mass-specific forward CV segments of NPG-Pt_1-Au_x catalysts in 0.1 M $HClO_4$ and 0.05 M HCOOH (after [21.136])

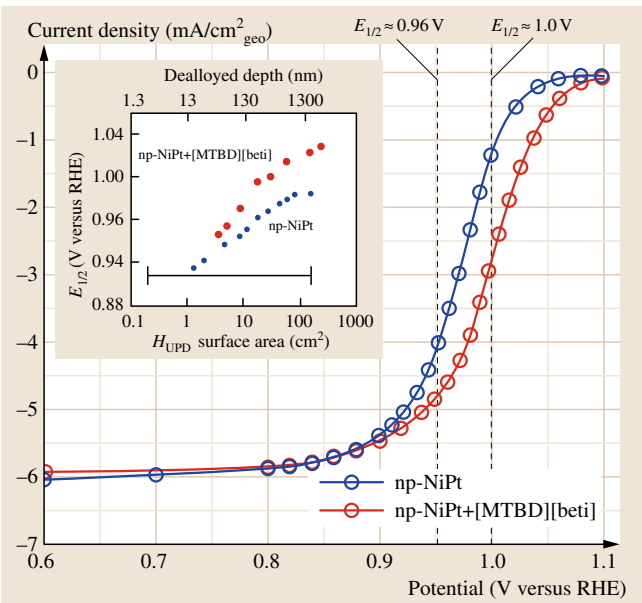

a consequence of the macroscopic structure. *Biener* et al. [21.150] reported on the fracture behavior of NPG with an open sponge-like morphology of interconnecting ligaments on the nanometer length scale. Despite its macroscopic brittleness, NPG is microscopically a very ductile material, as ligaments strained by as much as

Fig. 21.23 Potentiostatic ORR curves and half-wave as a function of roughness factor. np-NiPt (*red*) and np-NiPt+ [MTBD][beti] (*blue*) electrodes in O_2-saturated 0.1 M $HClO_4$ at 25 °C ($R_f = 143$ for all electrodes) with disc electrode rotation rate of 1600 rpm. Potentiostatic current measures were made at the indicated potential values (*circles*). *Inset*: Half-wave potential for both np-NiPt and composite np-NiPt + [MTBD][beti] as a function of H_{UPD} surface area, dealloyed depth, and roughness factor (R_f) (RHE = reversible hydrogen electrode; [MTBD][beti] = [7-methyl-1,5,7-triazabicyclo[4.4.0]dec-5-ene][bis(perfluoroethylsulfonyl)imide]) (after [21.146])

◀

200% can be observed in the vicinity of crack tips. Cell-size effects on the microscopic failure mechanism were studied by annealing treatments that increased the typical pore size/ligament diameter from 100 nm to 1 μm. Ligaments with diameter of 100 nm fail by plastic flow and necking, whereas failure by slip was observed for larger ligaments with diameter of 1 μm. The absence of slip marks in 100 nm-sized ligaments suggests strongly suppressed dislocation activity, consistent with the high yield strength of NPG. They also investigated the plastic deformation of NPG under compressive stress by depth-sensing *nanoindentation* [21.151]. Mean hardness of 145 ± 11 MPa was reported for the investigated NPG with a length scale of 100 nm, which is 10 times higher than the hardness predicted by scaling laws of open-cell foams. *Volkert* et al. [21.152] investigated the mechanical properties of NPG by uniaxial compression. Micrometer-sized columns were machined in the surface of NPG using a focused Ga^+ beam and compressed with a flat punch in a nanoindenter. Using scaling laws for foams, the yield strength of the 15 nm-diameter ligaments was estimated to be 1.5 GPa, close to the theoretical strength of Au. This value agrees well with extrapolations of the yield strength of submicron, fully dense gold columns and shows that, in addition to foam density and structure, the absolute size of ligaments and cell walls can be used to tailor foam properties. *Hodge* et al. [21.153] systematically investigated the mechanical properties of NPG with a wide range of ligament sizes and densities, and concluded that (a) NPG has a fracture behavior dictated by the ligament size, and (b) NPG is a high-yield-strength material.

Biener et al. [21.155] further demonstrated that nanoporous metals can be envisioned as a three-dimensional network of ultrahigh-strength nanowires, thus bringing together two seemingly conflicting properties: high strength and high porosity. They characterized the size-dependent mechanical properties of NPG using a combination of nanoindentation, column microcompression, and molecular dynamics simulations. They found that NPG can be as strong as bulk Au, despite being a highly porous material, and that the ligaments in NPG approach the theoretical yield strength of Au. *Mathur* and *Erlebacher* [21.156] determined the Young's modulus of NPG with controlled porosity variation between 3 and 40 nm by mechanical testing of ≈ 100 nm-thick, free-standing, large-grained, stress-free films of NPG using a buckling-based method. Their results show a dramatic rise in the effective Young's modulus of NPG with decreasing ligament size, especially below 10 nm. *Hodge* et al. [21.154] performed depth-sensing nanoindentation tests on NPG ranging from 20% to 42% relative density with ligament sizes ranging from 10 to 900 nm. The Gibson and Ashby yield strength equation for open-cell macrocellular foams was modified to incorporate ligament size effects. Their study demonstrated that, at the nanoscale, foam strength is governed by ligament size, in addition to relative density (Fig. 21.24). Furthermore, the ligament length scale was presented as a new parameter to tailor foam properties and achieve high strength at low densities. Later, *Hodge* et al. [21.157] studied the effect of Ag and the relative density on the elastic properties of NPG by depth-sensing nanoindentation. It was observed that the effect of the relative density on the elastic properties of NPG seems to be much stronger than predicted by the Gibson and Ashby relationship. Even Ag contents as low as 1 at. % can significantly change the modulus values. On the other hand, the elastic modulus of NPG seems to be independent of the ligament size.

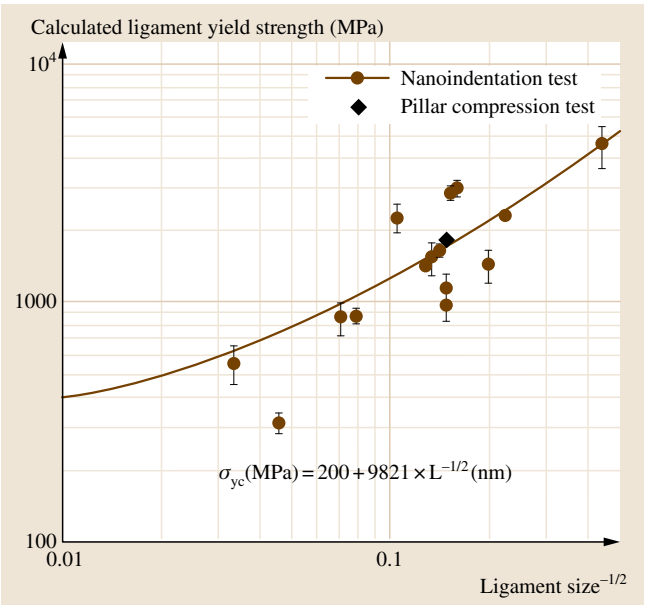

Fig. 21.24 Relationship of ligament size to ligament yield stress for nanoporous gold obtained by nanoindentation and by column microcompression testing (after [21.154])

Lee et al. [21.158] fabricated a free-standing dog-bone-shaped specimen with a gage section 7 μm long, 300 nm wide, and 100 nm thick, from NPG by dealloying *white gold* leaf ($Au_{37.4}Ag_{62.6}$ in [at.] %). The elastic modulus, residual stress, and yield stress were measured by deflective tensile testing and nanoindentation to be about 9 GPa, 65 MPa, and 110 MPa, respectively.

According to scaling laws, they further determined the yield stress within an individual ligament to be as high as 1.45 GPa, which approaches the theoretical shear strength of the material at which adjacent atomic planes slide past one another without the mediating influence of dislocations [21.159].

Seker et al. [21.160] investigated the effects of postfabrication annealing on the mechanical properties of free-standing nanoporous gold structures. Mechanical properties were measured using combinations of free-standing beam deflection, wafer curvature, and nanoindentation. The relative density of all sample geometries increased as the annealing temperature was increased. However, the evolution of the average pore size (with annealing) depended on the geometry, and hence on the boundary conditions, of the specimen. Differences in porosity evolution were reflected in the mechanical property measurements: while the elastic modulus and residual stress generally increased with increasing annealing temperature (due to densification), pore coalescence in films on substrates led to the most dramatic changes. Later, *Seker* et al. [21.161] studied the effects of annealing prior to dealloying on the mechanical properties of nanoporous gold microbeams. Normally, free-standing nanoporous gold beams fracture during dealloying owing to volume shrinkage. They found that annealing after release, yet prior to dealloying, prevents failure during the selective dissolution step. Experiments in which annealing was performed at temperatures $< 400\,^{\circ}\mathrm{C}$ illustrate that permanent buckling of the free-standing solid alloy beams is required to prevent failure of the nanoporous beams during dealloying. In contrast, annealing of beams prior to release, or annealing temperatures $< 200\,^{\circ}\mathrm{C}$ (which do not cause permanent buckling deformation), do not mitigate dealloying failures.

Jin et al. [21.162] recently reported on the fabrication and mechanical behavior of macroscopic, crack-free nanoporous gold samples which exhibit excellent ductility in compression tests. Their yield stress is significantly lower than that expected based on scaling laws or on previous nanoindentation experiments. Electron backscatter diffraction imaging reveals a polycrystalline microstructure with grains larger than 10 μm, which acquire a subdomain structure during plastic flow but remain otherwise intact. They highlighted the action of lattice dislocations which can travel over distances much larger than the ligament size. This results in collective deformation of the many ligaments in each grain. Remarkably, the dislocation cores are partly located in the pore channels. Their results suggest a critical view of the conversion between indentation hardness and yield stress in previous work.

The selection of a structural material requires a compromise between strength and ductility. Materials design strategies that allow for recoverable tuning of the mechanical properties would thus be desirable, either in response to external control signals or in the form of spontaneous adaptation, for instance, in self-healing. Most recently, *Jin* and *Weissmüller* [21.163] designed a material that has a hybrid nanostructure consisting of a strong metal backbone that is interpenetrated by an electrolyte as the second component. By polarizing the internal interface via an applied electric potential, they accomplished fast and repeatable tuning of yield strength, flow stress, and ductility (Fig. 21.25). Their results thus allow the user to select, for instance, a soft and ductile state for processing and a high-strength state for service as a structural material.

21.2.5 Optical Properties

Maaroof et al. [21.164] used ellipsometry and spectrophotometry to study the optical properties of mesoporous gold films obtained by dealloying of Al_2Au precursor. The complex refractive indices of the optically equivalent uniform smooth layer satisfy Kramers–Kronig (KK) self-consistency but have unusual dispersion relations and magnitudes for a film containing the amount of noble metal present. Mesoporous gold films exhibit unique dispersion in their optical response across all near-infrared (NIR) wavelengths. The effective optical constants as a function of wavelength, which are physically acceptable from a dispersion viewpoint, are neither metal nor insulator like. This is in effect a quite new class of optical material.

Later, *Maaroof* et al. [21.165] investigated and modeled the far-field plasmonic behavior of nanoporous gold films with void densities ranging from 60% to 90%. These layers have good direct-current (DC) conductivity and quite different nanostructure from traditional porous layers in which the metal percolates. Gold films with void density f above 70% have high thermal emittance for a conductor of their thicknesses, and their flat spectral response at visible and near-infrared wavelengths is not metal like. They derived effective optical constants which become plasmonic at wavelengths between 1.8 and 4 μm for f from 72% to 87%. This onset is much longer than that in bulk gold. For void densities below 70%, the onset of plasmonic behavior is much closer to the dense material. A test was implemented for surface plasmon polaritons (SPPs)

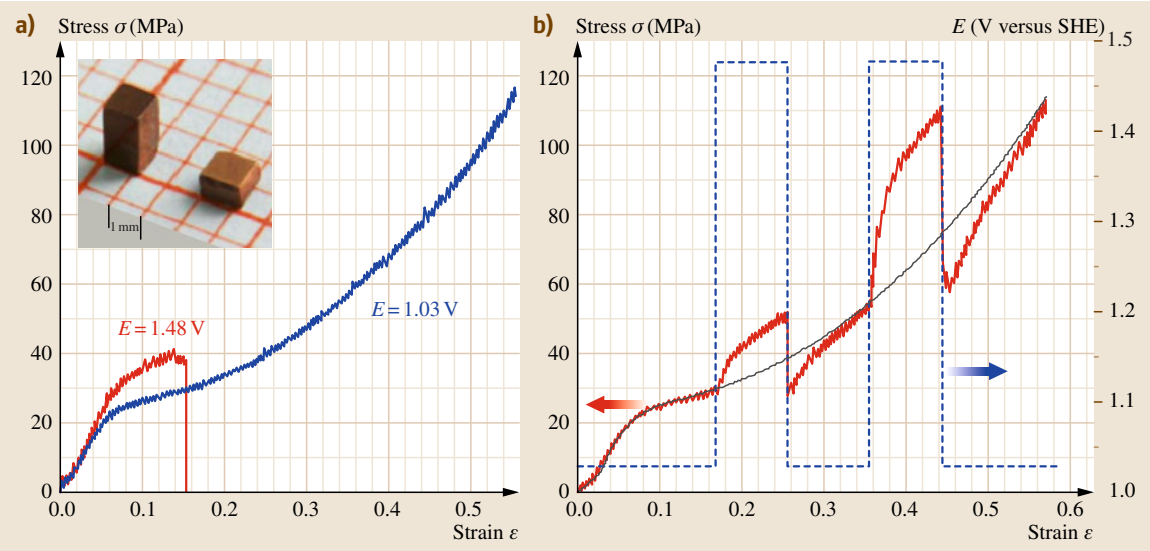

Fig. 21.25a,b Potential dependence of strength and flow stress of NPG. **(a)** Compressive stress–strain curves of engineering stress σ, versus engineering strain ε, measured in situ at constant potentials. Ligament surface is covered with submonolayer-thick oxygen when $E = 1.48$ V and is clean when potential is held at 1.03 V. The *inset* is a photograph of NPG samples with clean surface before and after compression. **(b)** Responses of plastic flow (*red*) to potential jumps. Data obtained at constant potential of 1.03 V (*gray*) were plotted for comparison (SHE = standard hydrogen electrode) (after [21.163])

under illumination. The more porous films show no evidence of SPP, while the less porous films display weak evidence. Thus, by tailoring the void content in these nanostructures, one can tailor the onset of effective plasmonic response across a wide range from 0.8 to 4 μm and emittance from around 0.9 down to low values. An effective uniform metal response was thus found in the presence of surface nanostructure without the interface absorption found in dense gold layers with structured surfaces.

Materials multifunctionality for optical sensing of adsorbates has obvious advantages: in addition to the potential for greater sensitivity, the different length scales associated with a variety of optical phenomena allow a greater variety of adsorption characteristics to be examined. *Yu* et al. [21.166] demonstrated that ultrathin (100 nm) nanoporous gold membranes possess features of both planar metal films that exhibit propagating surface plasmon resonance (SPR) excitations and nanofeatured metals that exhibit localized SPR excitations. They gave illustrative examples of using this material to probe biorecognition reactions and to probe the structure evolution of layer-by-layer deposition of charged dendrimers. Their results are consistent with the very different lengths of the tail of the evanescent field decays associated with each of these plasmon excitation modes. Later, they quantified the plasmonic properties of NPG through direct comparison with thermally evaporated gold (EG) films [21.167]. Cyclic voltammetry and electrochemical impedance spectroscopy experiments reveal that the NPG films have 4–8.5 times more accessible surface area than EG films. Assemblies of streptavidin–latex beads generate p-SPR responses on both NPG and EG films that correlate well with the bead density obtained from SEM images. A layer-by-layer assembly experiment on NPG involving biotinylated anti-avidin IgG and avidin, studied by l-SPR and SEM, showed that the l-SPR signal is directly linked to the accessibility of the interior of the NPG porosity.

Tuning of the localized surface plasmon resonance (l-SPR) of nanoporous metals lies at the heart of manipulating light within extremely small volumes for the implementation of optical devices at the nanoscale. *Qian* et al. [21.168] deposited amorphous alumina on chemically etched nanoporous gold films using atomic layer deposition at room temperature. Nanoporous gold with ultrafine pores of 7 nm diameter was uniformly coated with alumina film as thin as 1.4 nm. l-SPR of the gold skeleton exhibits a detectable red-shift

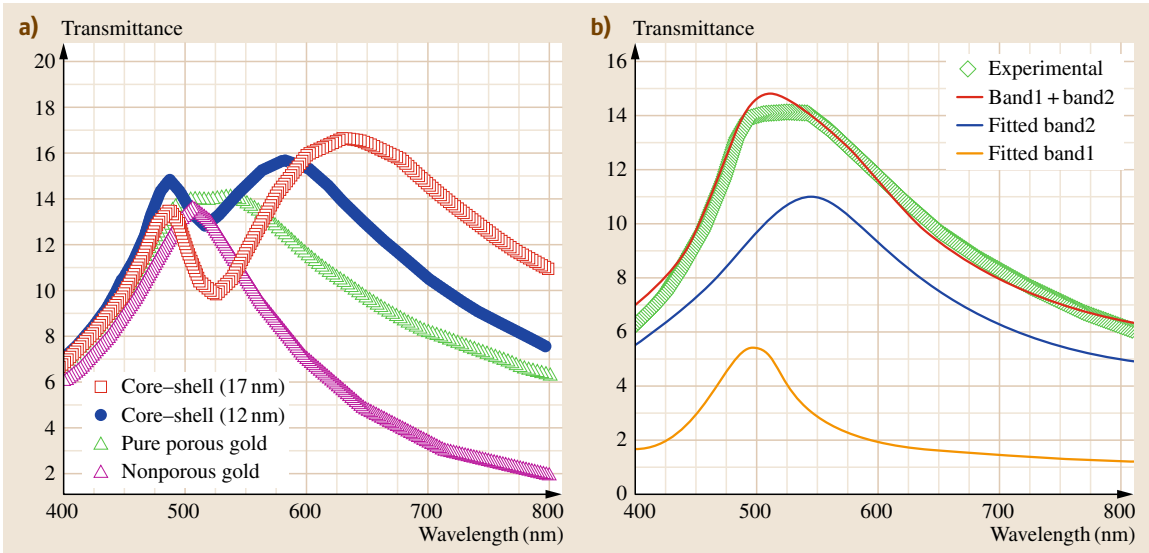

Fig. 21.26 **(a)** Transmittance spectra of nanoporous gold and nanoporous gold–alumina film with different shell thicknesses. The transmittance spectrum of 100 nm-thick gold film without pores is plotted for comparison. **(b)** Fitted spectrum of nanoporous gold indicates two isolated bands at 492 and 537 nm (after [21.169])

in the optical transmittance spectra, the magnitude of which depends on the thickness of the alumina layer. They further investigated the optical properties of nanoporous gold–alumina core–shell films with fixed gold skeletons and different thicknesses of alumina shells [21.169]. Optical transmission of the nanoporous composite films can be tailored through l-SPR excitations of the three-dimensional gold skeleton and the alterable alumina shells as the covering dielectric. A 92 nm red-shift of the l-SPR band is attained via its dielectric medium dependence and the comparable decay length with pore size (Fig. 21.26). The widely tunable optical transmission and significantly improved stability thus suggest incorporating nanoporous gold–alumina into promising nanodevices with reliable performance. Low-temperature surface decoration ($< 100\,^{\circ}\mathrm{C}$) provides a universal route to tune the optical properties while retaining the spatial geometry of the metallic nanostructures.

Surface-enhanced Raman scattering (SERS) originates from the improved inelastic scattering of molecules adsorbed on nanostructured metals and alloys. The SERS enhancements generally depend on the nanoscale characteristics of the metallic substrates, such as surface morphology, size, and aggregation state of nanoparticles. Nanoporous gold with excellent thermal stability and chemical inactivity has recently been exploited as an attractive substrate for SERS applications because of its large surface area and bicontinuous porous structure in three dimensions. *Kucheyev* et al. [21.170] reported that NPG with average pore widths of 250 nm exhibits the largest SERS signal for 632.8 nm excitation. They attributed this to the electromagnetic SERS enhancement mechanism with additional field localization within pores. *Dixon* et al. [21.171] prepared thin nanoporous gold films, ranging in thickness from 40 to 1600 nm, by selective chemical etching of Ag from Ag/Au alloy films supported on planar substrates. Raman scattering measurements for films functionalized with a self-assembled monolayer formed from 4-fluorobenzenethiol show significant enhancements which vary sharply with film thickness and etching times. The maximum enhancement factors reach $\approx 10^4$ for 632.8 nm excitation, peak sharply in the 200 nm thickness range for films prepared at optimum etching times, and show high spot-to-spot reproducibility with $\approx 1\,\mu\mathrm{m}$ laser spot sizes.

Chen's group at the Tohoku University carried out very systematic studies of the SERS behaviors of nanoporous metals. They found that the high SERS of nanoporous gold actually results from smaller microstructure features, either smaller pore sizes or the rough gold ligament surfaces, which are believed to promote electromagnetic field enhancements and provide more active sites for molecule adsorption. Moreover, the strongest SERS enhancement of nanoporous gold

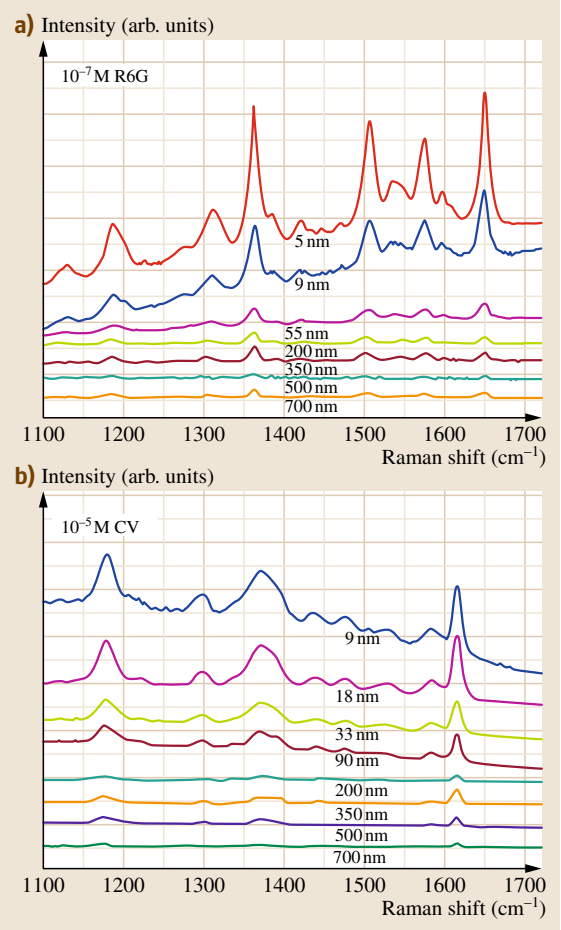

Fig. 21.27a,b SERS spectra of nanoporous gold with different pore sizes for **(a)** 10^{-7} mol/l R6G aqueous solution and **(b)** 10^{-5} mol/l CV methanol solution. Laser excitation: 514.5 nm for R6G and 632.8 nm for CV (CV = crystal violet 10B, R6G = rhodamine 6G) (after [21.172])

takes place for samples with ultrafine nanopore size of 5–10 nm (Fig. 21.27) [21.172]. The SERS intensities from the fracture surfaces of nanoporous gold are about one order of magnitude higher than those from the as-prepared samples [21.173]. Microstructural characterization reveals that the fracture surfaces contain numerous sharp protrusions with 5–10 nm apexes, produced by localized plastic deformation of gold ligaments during failure. They also reported a geometric effect on surface-enhanced Raman scattering of nanoporous gold and found that Raman scattering can be improved by tailoring ligament and nanopore ratios [21.174]. They studied SERS of NPG with various nanopore sizes at temperatures ranging from 80 to 300 K using rhodamine 6G (R6G) as probe molecule. It was found that the SERS intensity dramatically increases as temperature and nanopore size decrease. The improved SERS enhancements result from the combined effects of electron–phonon scattering, the finite ligament size effect, and the electromagnetic coupling between neighboring gold ligaments [21.175]. Moreover, the tunable nanoporosity leads to significant improvements in SERS of nanoporous copper, and peak values of SERS enhancements for both rhodamine 6G and crystal violet 10B (CV) molecules are observed at pore size of 30–50 nm [21.176]. In addition, silver on nanoporous copper core–shell composites also exhibit a dramatically improved SERS effect compared with that of the as-prepared nanoporous copper, and the enhancement factor strongly depends on the reaction time and Ag shell thickness [21.177]. Recently, *Qian* et al. [21.178] reported giant Raman enhancement on nanoporous gold film by conjugating with nanoparticles for single-molecule detection.

Lang et al. [21.179] reported molecular fluorescence enhancement of free-standing nanoporous gold with tunable nanopore size. They found that the fluorescence intensity of indocyanine green adsorbed on human-serum-albumin-coated nanoporous gold films significantly increases with decreasing nanopore size. The large fluorescence enhancement results from the near-field enhanced excitation and radioactive decay rate of fluorophore due to the strong electromagnetic fields produced by nanosized curvatures as well as the coupling between neighboring gold ligaments. By the combination of dealloying and electroless gold plating, they further tailored molecular fluorescence enhancement of free-standing nanoporous gold [21.180]. The nanoporous gold fabricated by this facile method possesses unique porous structures with large gold ligaments and very small pores, and exhibits significant improvements in surface-enhanced fluorescence as well as structure rigidity.

21.2.6 Sensing and Actuation Properties

Chou et al. [21.181] reported a nonenzymatic sensor using a nanoporous platinum electrode to detect glucose directly. The electrode was fabricated by electrochemical deposition and dissolution of Pt-Zn alloy in zinc chloride-1-ethyl-3-methylimidazolium chloride ($ZnCl_2$-EMIC) ionic liquid. Amperometric measurements allowed observation of the electrochemical oxidation of glucose at 0.4 V (versus Ag/AgCl) in pH 7.4

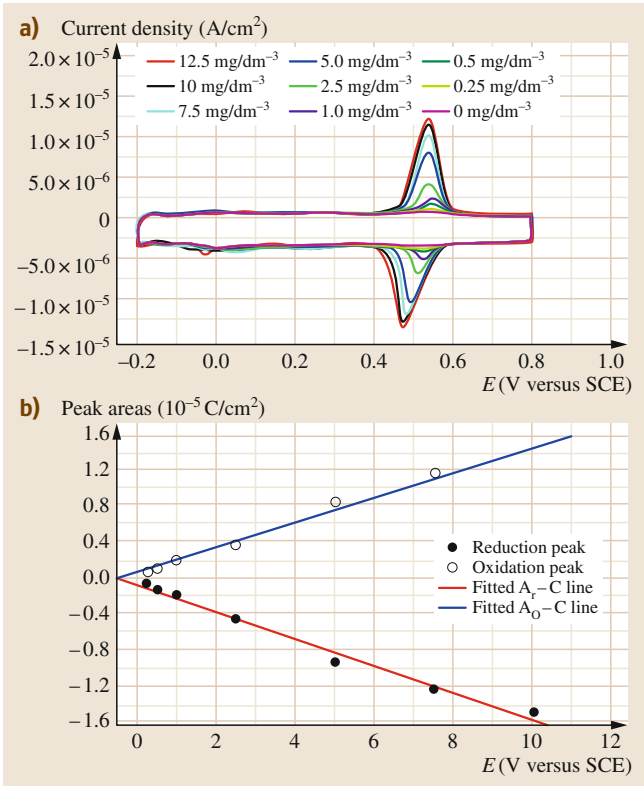

Fig. 21.28 **(a)** CVs for NPG electrode in 0.1 mol/dm^3 H_2SO_4 containing various concentrations of *p*-NP at 50 mV/s. **(b)** The linear dependence of redox peak areas on *p*-NP concentrations (after [21.182])

phosphate buffer solution. The sensor also demonstrates significant reproducibility in glucose detection; the higher the roughness factor of the Pt electrode, the lower the detection limit of glucose. Interfering species such as ascorbic acid and *p*-acetamidophenol can be avoided by using a Pt electrode with a high roughness factor of 151. Overall, the nanoporous Pt electrode is promising for enzymeless detection of glucose at physiological condition.

Qiu et al. [21.183, 184] have shown that nanoporous metals would be very good supports for immobilization of enzymes such as laccase, horseradish peroxidase (HRP), etc. Laccase was immobilized on the surface of NPG by physical adsorption. Laccase immobilized on NPG (100 nm in thickness) was used for enzyme electrode construction. Direct electrochemistry of laccase on NPG supported by glassy carbon electrode (NPG/GC) was achieved with high efficiency due to the outstanding physicochemical characteristics of the NPG. HRP can be immobilized on nanoporous copper by adsorption. Compared with free enzyme, the thermal stability of the immobilized enzyme was greatly improved due to the multiple attachments between the enzyme molecule and the nanoporous copper surface. Moreover, the HRP immobilized nanoporous electrode shows excellent sensing properties for electrochemical detection of *O*-phenylenediamine (OPD).

Liu et al. [21.182] used NPG samples as the working electrode to investigate the redox behavior of *p*-nitrophenol (*p*-NP) by cyclic voltammetry (CV). Quite different from the voltammetric behavior of polycrystalline gold electrode, the CV profiles of NPG display a pair of nearly symmetric redox waves which are ascribed to the reaction of the 4-(hydroxyamino)phenol/4-nitrosophenol couple. They also found that this pair of redox waves are hardly affected by the isomers of *p*-NP; and moreover, their peak areas are linear with the concentration of *p*-NP in the range from 0.25 to 10 mg/dm^3 (Fig. 21.28). Because of high sensitivity and good selectivity, NPG is expected to act as a promising electrochemical sensor material for detecting trace *p*-NP in wastewaters.

Most recently, *Ge* et al. reported that ultrathin freestanding nanoporous gold leaf made by dealloying exhibits excellent electrocatalytic activities toward nitrite oxidation [21.185]. The electrochemical response of nitrite ions on this novel nanoelectrode is found to be independent of pH over a wide range from 4.5 to 8.0, which is markedly different from that of gold oxidation, a process known to be highly pH sensitive. Amperometric study shows a linear relationship for nitrite determination in a concentration range from 1 μM to 1 mM. This nanostructured gold electrode displays good stability, repeatability, and selectivity, suggesting its potential for the development of new electrochemical sensors.

Although actuation in biological systems is exclusively powered by chemical energy, this concept has not been realized in manmade actuator technologies, as these rely on generating heat or electricity first. *Biener* et al. [21.186] have recently demonstrated that surface-chemistry-driven actuation can be realized in high-surface-area materials such as nanoporous gold. They achieved reversible strain amplitudes of the order of a few tenths of a percent by alternating exposure of nanoporous Au to ozone and carbon monoxide. The effect has been explained by adsorbate-induced changes of the surface stress, and can be used to convert chemical energy directly into a mechanical response, thus opening the door to surface-chemistry-driven actuator and sensor technologies. *Jin* et al. [21.187] fabricated

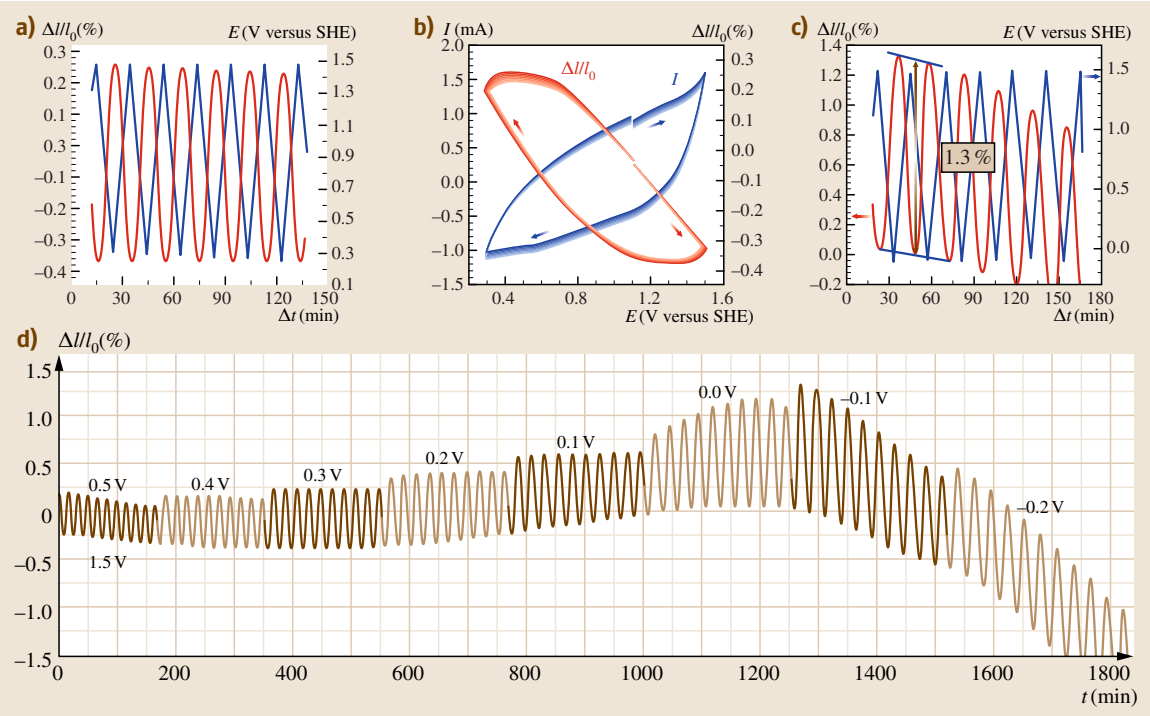

Fig. 21.29a–d Dilatometry experiments on an as-dealloyed nanoporous $Au_{0.8}Pt_{0.2}$ sample (with oxygen covered surface), in 0.7 M NaF solution. **(a)** Cyclic length change along with the potential sweep (10 successive scans) between 0.3 and 1.5 V. **(b)** The voltammogram and the reversible strain. **(c)** Cyclic length change along with the potential sweep between −0.1 and 1.5 V, showing largest strain up to 1.3%. **(d)** Cyclic length change during potential sweep. The upper vertex potential was fixed at 1.5 V. The lower vertex potential decreased by 100 mV after each 10 scans. The scan rate is 2 mV/s (after [21.187])

nanoporous Au-Pt alloys with pore and ligament size down to a few nanometers by dealloying Ag-Au-Pt. Owing to the small structure size and large specific surface area, the surface stress and its variation give rise to significant stress and strain in the bulk of these materials. Dilatometry experiments find electrochemical actuation with large reversible strain amplitude (Fig. 21.29). The linear strain reaches $\approx 1.3\%$, and the strain energy density is up to $6.0\,MJ/m^3$. The associated stresses may approach the elastic limit of the alloy. Their results show that nanoporous Au-Pt alloys are potential materials for use in large-strain electrochemical actuators.

21.2.7 Electrical, Thermal, and Magnetic Properties

Mishra et al. [21.188] measured the electrical conductivity of nanoporous gold in situ during charging and decharging of the surface of the metal. Charge was induced on the surface by making the sample a working electrode in an electrochemical cell. The conductivity was observed to vary reversibly with the induced surface charge. We have shown that the electrical resistivity of the nanoporous metals (Au, Ag, Cu) is one to two orders of magnitude higher than that of their bulk counterparts [21.60]. *Fujita* et al. [21.189] reported the electric conductivity of three-dimensional (3-D) nanoporous gold at low temperatures and in strong magnetic fields. It was found that topologically disordered 3-D nanoporosity leads to extremely low magnetoresistance and anomalous temperature dependence as the characteristic length of nanoporous gold is tuned to be 14 nm. Their study underscores the importance of the 3-D topology of a nanostructure on the electronic transport properties and has implications for manipulating electron transport by tailoring 3-D nanostructures.

Xia et al. [21.190] measured the thermal and electrical conductivities of nanoporous Au thin foils in the temperature range 93–300 K. Resulting from the nanoscale microstructure, the two types of conductivities are both temperature dependent and significantly lower than those of bulk Au. However, the corresponding Lorenz number is strikingly similar to that of bulk Au, indicating that the Wiedemann–Franz law holds perfectly well for nanoporous metals in this temperature range. Compared with the bulk value, the Debye temperature of nanoporous Au is decreased. The theoretical Debye temperature of nanoporous Au can be predicted by its relation to the elastic constants. The results indicate that the nanoporous Au foils should be comprised of macroscopic, single-crystalline porous grains rather than nanocrystals.

Wahl et al. [21.191] reported that the electrical resistance of nanoporous gold prepared by dealloying can be tuned by charging the surfaces of the porous structure in an electrolyte. Reversible variations in the resistance up to approximately 4% and 43% occur due to charging in the regimes of double-layer charging and specific adsorption, respectively. Charging-induced variations in the electron density or of the volume cannot account for the resistance variation, indicating that this variation is primarily caused by charge-induced modifications of the charge carrier scattering at the solid–electrolyte interface. The relative resistance variation in nanoporous Au with surface charging is found to be much higher than reported for porous nanocrystalline Pt. This is due to the lesser resistance contribution from internal grain boundaries. The resistance variation in nanoporous Au is also higher than that found in thin films owing to the stronger surface scattering in the ligament structure compared with plane surfaces. They argued that the strong resistance variation of up to 43% in the regime of specific adsorption is due to reversible formation of a chemisorbed surface layer acting as scattering centers for the charge carriers.

Sun et al. [21.59] reported that nanoporous nickel obtained by dealloying electrodeposited Ni_xCu_{1-x} alloys exhibits enhanced coercivity and reduced magnetic anisotropy. *Hakamada* et al. [21.192] reported that the coercivity of nanoporous Ni decreased with decreasing ligament length in a range below the critical size of about 50 nm. This trend for the nanoporous Ni is the same as those for nanoparticles and nanocrystals. However, the size dependence of coercivity for the nanoporous Ni is lower than those for the other materials. It is suggested that the dimension of the exchange length in the ligament is 1–2 for the nanoporous Ni, resulting in the low size dependence of coercivity. They also fabricated nanoporous Ni specimens with ligament lengths of 10–210 nm and specific surface areas of 0.03–0.58 nm^{-1} by dealloying of $Ni_{0.25}Mn_{0.75}$ alloy and annealing at 473–873 K, and investigated the saturation magnetization in terms of their size dependence [21.193]. Saturation magnetization decreased with decreasing ligament length or increasing specific surface area. This trend is the same as that for Ni nanoparticles. However, the saturation magnetization of nanoporous Ni tends to be lower than that of the Ni nanoparticles when their specific surface areas are the same. It is suggested, therefore, that the surface effect due to a noncollinear arrangement is enhanced by the surface defects in the nanoporous Ni.

21.3 Applications

Due to their unique mechanical, physical, and chemical properties associated with the 3-D bicontinuous interpenetrating ligament–channel structure, nanoporous metals show potential applications in the fields of fuel cells, sensors, actuators, supercapacitors, etc. Here, some examples are briefly summarized.

Increasingly stringent regulations on energy use and environmental protection lead to greater demands to commercialize clean energy-conversion technologies such as polymer electrolyte membrane fuel cells (PEMFCs). Considering that major obstacles remain for hydrogen mass production, storage, and transportation, direct methanol or formic acid fuel cells (DMFCs, DFAFCs) are gaining increasing attention. Therefore, there is growing interest in fabrication of effective electrocatalysts for formic acid and methanol electrooxidation, which is of great significance for commercialization of PEMFCs. One of the main obstacles to the commercialization of PEMFCs is the high cost of catalyst, which involves excess use of precious Pt. In comparison with nanoparticle catalysts supported on carbon black, platinum-coated NPG membranes simultaneously provide superior catalyst/substrate binding as well as high volume dispersion of catalyst, uniformly distributed through a very thin porous electrode with high in-plane conductivity [21.50]. Because the Pt load-

ing in platinum-plated nanoporous gold leaf (Pt-NPGL) can be controlled down to 0.01 mg/cm^2 using only simple benchtop chemistry, the material holds promise as a low-Pt-loading, carbon-free electrocatalyst [21.194]. Stable and high-performance Pt-NPGL/Nafion membrane electrode assemblies (MEAs) were made using a stamping technique by Zeis and coworkers. The performance of Pt-NPGL MEAs is comparable to conventional carbon-supported nanoparticle-based MEAs with much higher loading, generating output power density of up to 4.5 kW/g Pt in a nonoptimized test configuration. Through the construction of a novel NPG-Pt-Au nanostructure, superior performance of high activity and durability in electrocatalytic oxidation of formic acid was achieved at ultralow Pt loading down to microgram per unit-area scale [21.136]. Obviously, creating precious metal skins over nanoporous metal supports is a viable strategy for designing new catalysts for PEM fuel cells.

Chemisorption from the gas or liquid phase can result in a measurable resistance change in a metallic material when at least one dimension is smaller than the mean free path for electrons. *Liu* and *Searson* [21.196] reported on the fabrication of single nanoporous gold nanowires and demonstrated that adsorption of an alkanethiol can be monitored in real time. Single nanowire devices were fabricated by in situ etching of $Au_{0.18}Ag_{0.82}$ alloy nanowires in dilute nitric acid. The evolution of the porous structure was characterized by monitoring the resistance change and comparing with cross-sectional images. The feature size of about 10 nm is less than the mean free path for

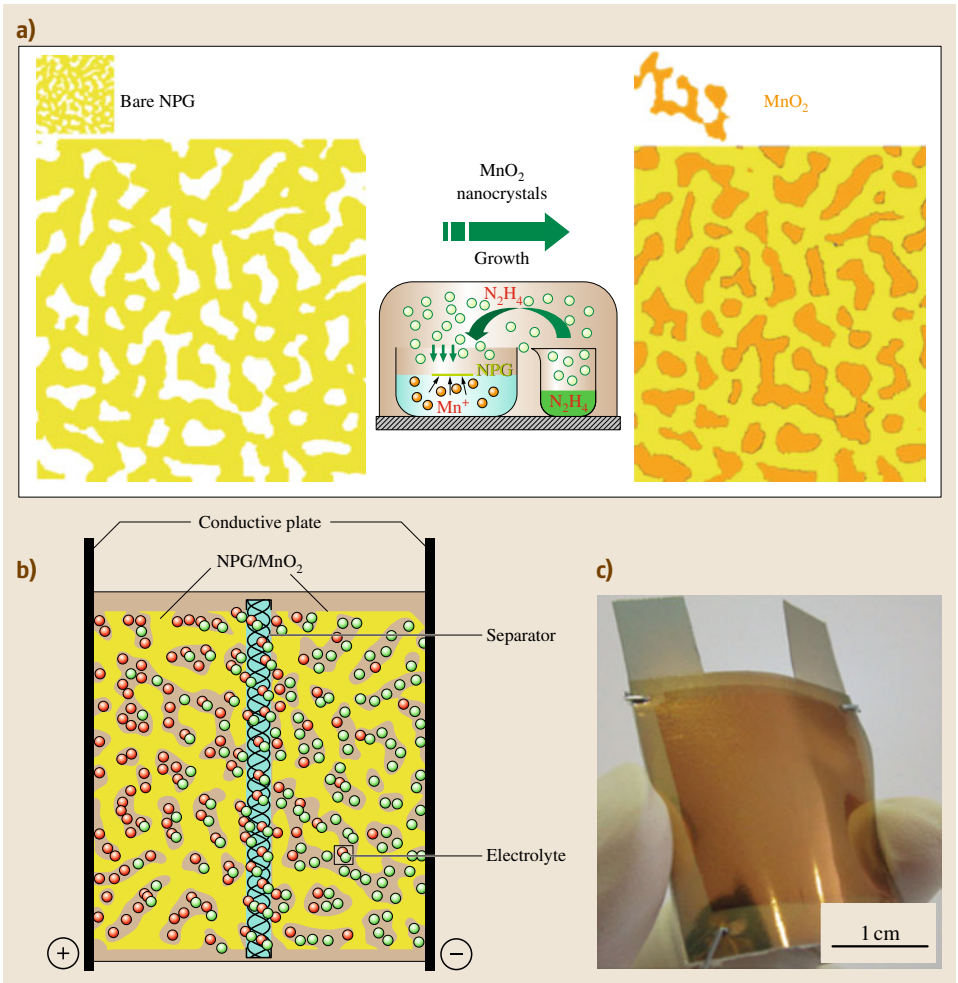

Fig. 21.30a–c Nanoporous gold/MnO_2-based supercapacitors. **(a)** Schematic showing the fabrication process for nanoporous gold/MnO_2 hybrid materials by directly growing MnO_2 (*orange*) onto nanoporous gold. **(b)** Supercapacitor device constructed with nanoporous gold/MnO_2 films as electrodes, aqueous Li_2SO_4 as electrolyte, and tissue paper as separator. **(c)** Photograph of a nanoporous gold/MnO_2-based supercapacitor (after [21.195])

electrons in bulk gold, and hence the resistance is dominated by surface scattering. Adsorption of a monolayer of octadecanethiol onto the nanoporous gold nanowire results in a resistance change of about 3%. The sensitivity factor of $1.0\times10^{-16}\,\mathrm{cm}^2$ is comparable to values reported for adsorption on ultrathin films.

Electrochemical supercapacitors can deliver high levels of electrical power and offer long operating lifetimes, but their energy storage density is too low for many important applications. Pseudocapacitive transition-metal oxides such as MnO_2 or SnO_2 could be used to make composite electrodes for such purposes, because they are predicted to have high capacitance for storing electrical charges while also being inexpensive and not harmful to the environment. However, the poor conductivity of MnO_2 (10^{-5}–$10^{-6}\,\mathrm{S/cm}$) limits the charge/discharge rate for high-power applications. Most recently, *Lang* et al. [21.195] showed that hybrid structures made of nanoporous gold and nanocrystalline MnO_2 have enhanced conductivity, resulting in a specific capacitance of the constituent MnO_2 ($\approx 1.145\,\mathrm{F/g}$) that is close to the theoretical value. The nanoporous gold allows electron transport through the MnO_2, and facilitates fast ion diffusion between the MnO_2 and the electrolytes while also acting as a double-layer capacitor (Fig. 21.30). The high specific capacitances and charge/discharge rates offered by such hybrid structures make them promising candidates as electrodes in supercapacitors, combining high energy storage densities with high levels of power delivery.

21.4 Concluding Remarks and Prospects

Nanoporous metals with three-dimensional bicontinuous ligament–channel structure can be fabricated by chemical or electrochemical dealloying, which involves selective dissolution of the less noble element and surface diffusion/agglomeration of the more noble element. The length scale of the ligaments and channels in nanoporous metals ranges from a few nanometers to several microns, and can be tuned by changing parameters such as the composition and microstructure of precursors, the applied potential, the kind and strength of the electrolyte, and the dealloying temperature and time, or by adopting post-dealloying treatments such as thermal annealing. By alloy design of precursors (addition of elements with lower surface diffusivity) and control over the applied dealloying potential or temperature, ultrafine pores of well below 10 nm can be achieved in nanoporous metals, which show enhanced SERS effects, superior catalytic activity towards CO oxidation, improved effective Young's modulus, etc. Both monoliths (films, ribbons, bulk) and nanostructures (nanoparticles, nanowires, nanotubes) can be obtained for nanoporous metals. Besides pure metals (containing a minor residue of the less noble element), nanoporous alloys can be produced by dealloying ternary or multicomponent precursors. Moreover, one can continuously modulate the compositions of these nanoporous alloys. Through combination with other routes such as the template method, UPD deposition, etc., dealloying provides more space to tailor the microstructure of nanoporous metal materials. Due to the bicontinuous porous structure and ultrahigh specific surface area, nanoporous metals show unique mechanical, catalytic, electrocatalytic, optical, electrical, sensing, and actuation properties, compared with their dense bulk counterparts or nonporous nanostructures; for example, the tunable length scale of ligaments and channels allows for investigation of the size-dependent mechanical behavior of nanoporous metals. The ultrahigh specific surface area is desirable for high sensitivity, and the 3-D channels contribute to fast transfer of adsorption species and shorter response time for applications of sensors. This point is also desirable for electrocatalysis in fuel cell applications. On the one hand, nanoporous metals can serve as model materials for investigations of mechanical, physical, and chemical properties of random porous solids, from the viewpoint of fundamental science; On the other hand, from the technological viewpoint, nanoporous metals show potential applications in many fields such as catalysis, electrocatalysis, sensors, actuators, fuel cells, supercapacitors, etc. It is expected that more and more fascinating properties of dealloyed nanoporous metals will soon be uncovered, as well as their tremendous potential for actual applications.

References

21.1 V. Bansal, H. Jani, J.D. Plessis, P.J. Coloe, S.K. Bhargava: Galvanic replacement reaction on metal films: A one-step approach to create nanoporous surfaces for catalysis, Adv. Mater. **20**, 717–723 (2008)

21.2 A. Kiani, E. Nekooiy Fard: Fabrication of palladium coated nanoporous gold film electrode via underpotential deposition and spontaneous metal replacement: A low palladium loading electrode with electrocatalytic activity, Electrochim. Acta **54**, 7254–7259 (2009)

21.3 J.F. Huang: Facile preparation of an ultrathin nickel film coated nanoporous gold electrode with the unique catalytic activity to oxidation of glucose, Chem. Commun. **10**, 1270–1272 (2009)

21.4 Y. Wang, C.C. He, W.H. Xing, F.B. Li, L. Tong, Z.Q. Chen, X.Z. Liao, M. Steinhart: Nanoporous metal membranes with bicontinuous morphology from recyclable block-copolymer templates, Adv. Mater. **22**, 2068–2072 (2010)

21.5 H. Ataee-Esfahani, N. Fukata, Y. Yamauchi: Templateless synthesis of nanoporous gold sponge with surface-enhanced Raman scattering activity, Chem. Lett. **39**, 372–373 (2010)

21.6 D.B. Robinson, S.J. Fares, M.D. Ong, I. Arslan, M.E. Langham, K.L. Tran, W.M. Clift: Scalable synthesis of nanoporous palladium powders, Int. J. Hydrogen Energy **34**, 5585–5591 (2009)

21.7 X.S. Peng, K. Koczkur, S. Nigro, A.C. Chen: Fabrication and electrochemical properties of novel nanoporous platinum network electrodes, Chem. Commun. **24**, 2872–2873 (2004)

21.8 X.S. Peng, K. Koczkur, A.C. Chen: Synthesis and characterization of ruthenium-decorated nanoporous platinum materials, Nanotechnology **18**, 305605 (2007)

21.9 Q.F. Yi, W. Huang, X.P. Liu, G.R. Xu, Z.H. Zhou, A.C. Chen: Electroactivity of titanium-supported nanoporous Pd-Pt catalysts towards formic acid oxidation, J. Electroanal. Chem. **619/620**, 197–205 (2008)

21.10 A.K.M. Kafi, A. Ahmadalinezhad, J.P. Wang, D.F. Thomas, A.C. Chen: Direct growth of nanoporous Au and its application in electrochemical biosensing, Biosens. Bioelectron. **25**, 2458–2463 (2010)

21.11 Q.F. Yi, W.Q. Yu, F.J. Niu: Novel nanoporous binary Au_Ru electrocatalysts for glucose oxidation, Electroanalyst **22**, 556–563 (2010)

21.12 J. Kim, Z. Dohnálek, B.D. Kay: Structural characterization of nanoporous Pd films grown via ballistic deposition, Surf. Sci. **586**, 137–145 (2005)

21.13 C. Bansal, S. Sarkar, A.K. Mishra, T. Abraham, C. Lemier, H. Hahn: Electronically tunable conductivity of a nanoporous Au–Fe alloy, Scr. Mater. **56**, 705–708 (2007)

21.14 J.R. Hayes, G.W. Nyce, J.D. Kuntz, J.H. Satcher, A.V. Hamza: Synthesis of bi-modal nanoporous Cu, CuO and Cu_2O monoliths with tailored porosity, Nanotechnology **18**, 275602 (2007)

21.15 Y.P. Deng, W. Huang, X. Chen, Z.L. Li: Facile fabrication of nanoporous gold film electrodes, Electrochem. Commun. **10**, 810–813 (2008)

21.16 K. Nishio, H. Masuda: Anodization of gold in oxalate solution to form a nanoporous black film, Angew. Chem. **123**, 1641–1645 (2011)

21.17 Y.J. Lee, D.J. Park, J.Y. Park: Fully packaged nonenzymatic glucose microsensors with nanoporous platinum electrodes for anti-fouling, IEEE Sens. J. **8**, 1922–1927 (2008)

21.18 J.B. Jia, L.Y. Cao, Z.H. Wang: Platinum-coated gold nanoporous film surface: Electrodeposition and enhanced electrocatalytic activity for methanol oxidation, Langmuir **24**, 5932–5936 (2008)

21.19 O.V. Shulga, D. Zhou, A.V. Demchenko, K.J. Stine: Detection of free prostate specific antigen (fPSA) on a nanoporous gold platform, Analyst **133**, 319–322 (2008)

21.20 B. Seo, J. Kim: Electrooxidation of glucose at nanoporous gold surfaces: Structure dependent electrocatalysis and its application to amperometric detection, Electroanalysis **22**, 939–945 (2010)

21.21 L.T. Viyannalage, Y. Liu, N. Dimitrov: Processing of nanoporous Ag layers by potential-controlled displacement (PCD) of Cu, Langmuir **24**, 8332–8337 (2008)

21.22 X.Y. Bu, J.H. Yuan, J.X. Song, D.X. Han, L. Niu: Controlled synthesis of nanoporous Au microsheet via surfactant emulsion template, Mater. Chem. Phys. **116**, 153–157 (2009)

21.23 Y. Du, J.J. Xu, H.Y. Chen: Ultrathin platinum film covered high-surface-area nanoporous gold (by anodization and subsequent reduction) for methanol electro-oxidation, Electrochem. Commun. **11**, 1717–1720 (2009)

21.24 H.J. Qiu, X.R. Huang: Effects of Pt decoration on the electrocatalytic activity of nanoporous gold electrode toward glucose and its potential application for constructing a nonenzymatic glucose sensor, J. Electroanal. Chem. **643**, 39–45 (2010)

21.25 R. Dou, B.J. Xu, B. Derby: High-strength nanoporous silver produced by inkjet printing, Scr. Mater. **63**, 308–311 (2010)

21.26 N.A. Luechinger, S.G. Walt, W.J. Stark: Printable nanoporous silver membranes, Chem. Mater. **22**, 4980–4986 (2010)

21.27 S.J. Guo, S.J. Dong, E. Wang: Ultralong Pt-on-Pd bimetallic nanowires with nanoporous surface: Nanodendritic structure for enhanced electrocatalytic activity, Chem. Commun. **46**, 1869–1871 (2010)

21.28 A.J. Forty: Corrosion micromorphology of noble metal alloys and depletion gilding, Nature **282**, 597–598 (1979)

21.29 A. Parthasarathi, N.W. Polan: Stress corrosion of Cu-Zn and Cu-Zn-Ni alloys: The role of dealloying, Metall. Trans. A **13**, 2027–2033 (1982)

21.30 K. Sieradzki, R.C. Newman: Stress-corrosion cracking, J. Phys. Chem. Solids **48**, 1101–1113 (1987)

21.31 H. Martín, P. Carro, A.H. Creus, J. Morales, G. Fernández, P. Esparza, S. González, R.C. Salvarezza, A.J. Arvia: Interplay of surface diffusion and surface tension in the evolution of solid/liquid interfaces. Dealloying of α-brass in aqueous sodium chloride, J. Phys. Chem. B **104**, 8229–8237 (2000)

21.32 F.M. Al-Kharafi, B.G. Ateya, R.M. Abd Allah: Selective dissolution of brass in salt water, J. Appl. Electrochem. **34**, 47–53 (2004)

21.33 M.B. Vukmirovic, N. Dimitrov, K. Sieradzki: Dealloying and corrosion of Al alloy 2024-T3, J. Electrochem. Soc. **149**, B428–B439 (2002)

21.34 Z. Han, Y.F. He, H.C. Lin, H. Zhao: Dealloying characterizations of Cu-Al alloy in marine environment, J. Mater. Sci. Lett. **19**, 393–395 (2000)

21.35 C.K. Lee, H.C. Shih: Effect of halide ions on electrochemical behavior and stress corrosion cracking of 67/33 α-brass in aqueous environments, Corrosion **52**, 690–696 (1996)

21.36 F. Mazza, S. Torchio: Factors influencing the susceptibility to intergranular attack, stress corrosion cracking and de-alloying attack of aluminium brass, Corros. Sci. **23**, 1053–1072 (1983)

21.37 J.S. Chen, M. Salmeron, T.M. Devine: Intergranular vs transgranular stress corrosion cracking of Cu 30-Au, Scri. Metall. Mater. **26**, 739–742 (1992)

21.38 J.G. Kim, S.B. Jung, O.H. Kwon: Dealloying behavior of unleaded brasses containing bismuth in potable water, Corrosion **57**, 291–294 (2001)

21.39 M.J. Pryor: The dealloying of a Cu-8.9% Al solid solution, J. Electrochem. Soc. **130**, 1625–1627 (1983)

21.40 K. Sieradzki, J.S. Kim, A.T. Cole, R.C. Newman: The relationship between dealloying and transgranular stress-corrosion cracking of Cu-Zn and Cu-Al alloys, J. Electrochem. Soc. **134**, 1635–1639 (1987)

21.41 M. Raney: US Patent 1563587 (1 Dec. 1925)

21.42 M. Raney: Catalysts from alloys, Ind. Eng. Chem. **32**, 1199–1203 (1940)

21.43 H.W. Pickering, P.R. Swann: Electron metallography of chemical attack upon some alloys susceptible to stress corrosion cracking, Corrosion **19**, 373–389 (1963)

21.44 P.R. Swann: Mechanism of corrosion tunnelling with special reference to Cu_3Au, Corrosion **25**, 147–150 (1969)

21.45 K. Sieradzki, R.C. Newman: Micro- and nanoporous metallic structures, US Patent 4977038 (11 Dec. 1990)

21.46 I.C. Oppenheim, D.J. Trevor, C.E.D. Chidsey, P.L. Trevor, K. Sieradzki: In situ scanning tunneling microscopy of corrosion of silver-gold alloys, Science **254**, 687–689 (1991)

21.47 R.C. Newman, K. Sieradzki: Corrosion science, MRS Bulletin **24**, 12–13 (1999)

21.48 J. Erlebacher, M.J. Aziz, A. Karma, N. Dimitrov, K. Sieradzki: Evolution of nanoporosity in dealloying, Nature **410**, 450–453 (2001)

21.49 Y. Ding, J. Erlebacher: Nanoporous metals with controlled multimodal pore size distribution, J. Am. Chem. Soc. **125**, 7772–7773 (2003)

21.50 Y. Ding, M.W. Chen, J. Erlebacher: Metallic mesoporous nanocomposites for electrocatalysis, J. Am. Chem. Soc. **126**, 6876–6877 (2004)

21.51 Y. Ding, Y.J. Kim, J. Erlebacher: Nanoporous gold leaf: "ancient technology"/advanced material, Adv. Mater. **16**, 1897–1900 (2004)

21.52 Y. Ding, A. Mathur, M.W. Chen, J. Erlebacher: Epitaxial casting of nanotubular mesoporous platinum, Angew. Chem. Int. Ed. **44**, 4002–4006 (2005)

21.53 J. Erlebacher: An atomistic description of dealloying: Porosity evolution, the critical potential, and rate-limiting behavior, J. Electrochem. Soc. **151**, C614–C626 (2004)

21.54 U.S. Min, J.C.M. Li: The microstructure and dealloying kinetics of a Cu-Mn alloy, J. Mater. Res. **9**, 2878–2883 (1994)

21.55 D.V. Pugh, A. Dursun, S.G. Corcoran: Formation of nanoporous platinum by selective dissolution of Cu from $Cu_{0.75}Pt_{0.25}$, J. Mater. Res. **18**, 216–221 (2003)

21.56 H.B. Lu, Y. Li, F.H. Wang: Dealloying behaviour of Cu–20Zr alloy in hydrochloric acid solution, Corros. Sci. **48**, 2106–2119 (2006)

21.57 J.R. Hayes, A.M. Hodge, J. Biener, A.V. Hamza: Monolithic nanoporous copper by dealloying Mn–Cu, J. Mater. Res. **21**, 2611–2616 (2006)

21.58 F.U. Renner, Y. Gründer, P.F. Lyman, J. Zegenhagen: In-situ X-ray diffraction study of the initial dealloying of $Cu_3Au(001)$ and $Cu_{0.83}Pd_{0.17}(001)$, Thin Solid Films **515**, 5574–5580 (2007)

21.59 L. Sun, C.L. Chien, P.C. Searson: Fabrication of nanoporous nickel by electrochemical dealloying, Chem. Mater. **16**, 3125–3129 (2004)

21.60 Z.H. Zhang, Y. Wang, Z. Qi, W.H. Zhang, J.Y. Qin, J. Frenzel: Generalized fabrication of nanoporous metals (Au, Pd, Pt, Ag, and Cu) through chemical dealloying, J. Phys. Chem. C **113**, 12629–12636 (2009)

21.61 Q. Zhang, Z.H. Zhang: On the electrochemical dealloying of Al-based alloys in a NaCl aqueous solution, Phys. Chem. Chem. Phys. **12**, 1453–1472 (2010)

21.62 C.C. Zhao, Z. Qi, X.G. Wang, Z.H. Zhang: Fabrication and characterization of monolithic nanoporous copper through chemical ealloying of Mg–Cu alloys, Corros. Sci. **51**, 2120–2125 (2009)

21.63 H. Ji, X.G. Wang, C.C. Zhao, C. Zhang, J.L. Xu, Z.H. Zhang: Formation, control and functionalization of nanoporous silver through changing

dealloying media and elemental doping, CrystEngComm. **13**, 2617–2628 (2011)
21.64 J.F. Huang, I.W. Sun: Fabrication and surface functionalization of nanoporous gold by electrochemcial alloying/dealloying of Au-Zn in an ionic liquid, and the self-assembly of L-Cysteine monolayers, Adv. Funct. Mater. **15**, 989–994 (2005)
21.65 F.H. Yeh, C.C. Tai, J.F. Huang, I.W. Sun: Formation of porous silver by electrochemical alloying/dealloying in a water-insensitive zinc chloride-1-ethyl-3-methyl imidazolium chloride ionic liquid, J. Phys. Chem. B **110**, 5215–5222 (2006)
21.66 Y.W. Lin, C.C. Tai, I.W. Sun: Electrochemical preparation of porous copper surfaces in zinc chloride-1-ethyl-3-methyl imidazolium chloride ionic liquid, J. Electrochem. Soc. **154**, D316–D321 (2007)
21.67 F. Jia, C.F. Yu, K.J. Deng, L.Z. Zhang: Nanoporous metal (Cu, Ag, Au) films with high surface area: General fabrication and preliminary electrochemical performance, J. Phys. Chem. C **111**, 8424–8431 (2007)
21.68 Z.H. Zhang, Y. Wang, Z. Qi, J.K. Lin, X.F. Bian: Nanoporous gold ribbons with bimodal channel size distributions by chemical dealloying of Al–Au alloys, J. Phys. Chem. C **113**, 1308–1314 (2009)
21.69 Z.H. Zhang, Y. Wang, Z. Qi, C. Somsen, X.G. Wang, C.C. Zhao: Fabrication and characterization of nanoporous gold composites through chemical dealloying of two phase Al-Au alloys, J. Mater. Chem. **19**, 6042–6050 (2009)
21.70 H.B. Lu, Y. Li, F.H. Wang: Synthesis of porous copper from nanocrystalline two-phase Cu–Zr film by dealloying, Scr. Mater. **56**, 165–168 (2007)
21.71 H. Ji, J. Frenzel, Z. Qi, X.G. Wang, C.C. Zhao, Z.H. Zhang, G. Eggeler: An ultrafine nanoporous bimetallic Ag–Pd alloy with superior catalytic activity, CrystEngComm. **12**, 4059–4062 (2010)
21.72 X.G. Wang, J. Frenzel, W.M. Wang, H. Ji, Z. Qi, Z.H. Zhang, G. Eggeler: Length – scale modulated and electrocatalytic activity enhanced nanoporous gold by doping, J. Phys. Chem. C **115**, 4456–4465 (2011)
21.73 J.S. Yu, Y. Ding, C.X. Xu, A. Inoue, T. Sakurai, M.W. Chen: Nanoporous metals by dealloying multicomponent metallic glasses, Chem. Mater. **20**, 4548–4550 (2008)
21.74 J.C. Thorp, K. Sieradzki, L. Tang, P.A. Crozier, A. Misra, M. Nastasi, D. Mitlin, S.T. Picraux: Formation of nanoporous noble metal thin films by electrochemical dealloying of Pt_xSi_{1-x}, Appl. Phys. Lett. **88**, 033110 (2006)
21.75 H.W. Pickering, C. Wagner: Electrolytic dissolution of binary alloys containing a noble metal, J. Electrochem. Soc. **114**, 698–706 (1967)
21.76 A.J. Forty, P. Durkin: A micromorphological study of the dissolution of silver – gold alloys in nitric acid, Philos. Mag. A **42**, 295–318 (1980)
21.77 A.J. Forty, G. Rowlands: A possible model for corrosion pitting and tunneling in noble – metal alloys, Philos. Mag. A **43**, 171–188 (1981)
21.78 K. Sieradzki, R. Corderman, K. Shukla, R.C. Newman: Computer simulations of corrosion: Selective dissolution of binary alloys, Philos. Mag. A **59**, 713–746 (1989)
21.79 F.U. Renner, A. Stierle, H. Dosch, D.M. Kolb, T.L. Lee, J. Zegenhagen: Initial corrosion observed on the atomic scale, Nature **439**, 707–710 (2006)
21.80 K. Wagner, S.R. Brankovic, N. Dimitrov, K. Sieradzki: Dealloying below the Critical Potential, J. Electrochem. Soc. **144**, 3545–3555 (1997)
21.81 C.C. Zhao, X.G. Wang, Z. Qi, H. Ji, Z.H. Zhang: On the electrochemical dealloying of Mg–Cu alloys in a NaCl aqueous solution, Corros. Sci. **52**, 3962–3972 (2010)
21.82 Q. Zhang, X.G. Wang, Z. Qi, Y. Wang, Z.H. Zhang: A benign route to fabricate nanoporous gold through electrochemical dealloying of Al–Au alloys in a neutral solution, Electrochim. Acta, **54**, 6190–6198 (2009)
21.83 X.G. Wang, Z. Qi, C.C. Zhao, W.M. Wang, Z.H. Zhang: Influence of alloy composition and dealloying solution on the formation and microstructure of monolithic nanoporous silver through chemical dealloying of Al-Ag alloys, J. Phys. Chem. C **113**, 13139–13150 (2009)
21.84 F.J. Lai, W.N. Su, L.S. Sarma, D.G. Liu, C.A. Hsieh, J.F. Lee, B.J. Hwang: Chemical dealloying mechanism of bimetallic Pt–Co nanoparticles and enhancement of catalytic activity toward oxygen reduction, Chem. Eur. J. **16**, 4602–4611 (2010)
21.85 Y. Liu, S. Bliznakov, N. Dimitrov: Factors controlling the less noble metal retention in nanoporous structures processed by electrochemical dealloying, J. Electrochem. Soc. **157**, K168–K176 (2010)
21.86 D.V. Pugh, A. Dursun, S.G. Corcoran: Electrochemical and morphological characterization of Pt-Cu dealloying, J. Electrochem. Soc. **152**, B455–B459 (2005)
21.87 A. Antoniou, D. Bhattacharrya, J.K. Baldwin, P. Goodwin, M. Nastasi, S.T. Picraux, A. Misra: Controlled nanoporous Pt morphologies by varying deposition parameters, Appl. Phys. Lett. **95**, 073116 (2009)
21.88 E. Seker, M.L. Reed, M.R. Begley: A thermal treatment approach to reduce microscale void formation in blanket nanoporous gold films, Scr. Mater. **60**, 435–438 (2009)
21.89 O. Okman, D. Lee, J.W. Kysar: Fabrication of crack – free nanoporous gold blanket thin films by potentiostatic dealloying, Scr. Mater. **63**, 1005–1008 (2010)
21.90 W.C. Li, T.J. Balk: Effects of substrate curvature on dealloying of nanoporous thin films, Scr. Mater. **61**, 1125–1128 (2009)

21.91 H.Q. Li, A. Misra, J.K. Baldwin, S.T. Picraux: Synthesis and characterization of nanoporous Pt–Ni alloys, Appl. Phys. Lett. **95**, 201902 (2009)

21.92 J. Snyder, K. Livi, J. Erlebacher: Dealloying silver/gold alloys in neutral silver nitrate solution: Porosity evolution, surface composition, and surface oxides, J. Electrochem. Soc. **155**, C464–C473 (2008)

21.93 E. Detsi, M. van de Schootbrugge, S. Punzhin, P.R. Onck, J.T.M. De Hosson: On tuning the morphology of nanoporous gold, Scr. Mater. **64**, 319–322 (2011)

21.94 W.C. Li, T.J. Balk: Achieving finer pores and ligaments in nanoporous palladium–nickel thin films, Scr. Mater. **62**, 167–169 (2010)

21.95 A. Dursun, D.V. Pugh, S.G. Corcoran: Dealloying of Ag–Au alloys in halide-containing electrolytes, affect on critical potential and pore size, J. Electrochem. Soc. **150**, B355–B360 (2003)

21.96 L.H. Qian, M.W. Chen: Ultrafine nanoporous gold by low-temperature dealloying and kinetics of nanopore formation, Appl. Phys. Lett. **91**, 083105 (2007)

21.97 Z.H. Zhang, Y. Wang, Y.Z. Wang, X.G. Wang, Z. Qi, H. Ji, C.C. Zhao: Formation of ultrafine nanoporous gold related to surface diffusion of gold adatoms during dealloying of Al_2Au in an alkaline solution, Scr. Mater. **62**, 137–140 (2010)

21.98 C.X. Xu, R.Y. Wang, M.W. Chen, Y. Zhang, Y. Ding: Dealloying to nanoporous Au/Pt alloys and their structure sensitive electrocatalytic properties, Phys. Chem. Chem. Phys. **12**, 239–246 (2010)

21.99 J. Snyder, P. Asanithi, A.B. Dalton, J. Erlebacher: Stabilized nanoporous metals by dealloying ternary alloy precursors, Adv. Mater. **20**, 4883–4886 (2008)

21.100 M. Hakamada, M. Mabuchi: Nanoporous gold prism microassembly through a self – organizing route, Nano Lett. **6**, 882–885 (2006)

21.101 C.X. Ji, P.C. Searson: Fabrication of nanoporous gold nanowires, Appl. Phys. Lett. **81**, 4437–4439 (2002)

21.102 L.Y. Chen, T. Fujita, Y. Ding, M.W. Chen: A three-dimensional gold-decorated nanoporous copper core-shell composite for electrocatalysis and nonenzymatic biosensing, Adv. Funct. Mater. **20**, 2279–2285 (2010)

21.103 X.B. Ge, X.L. Yan, R.Y. Wang, F. Tian, Y. Ding: Tailoring the structure and property of Pt-decorated nanoporous gold by thermal annealing, J. Phys. Chem. C **113**, 7379–7384 (2009)

21.104 S.G. Corcoran: The morphology of alloy corrosion, Proc. Electrochem. Soc. **3**, 1–8 (1998)

21.105 T. Fujita, M.W. Chen: Characteristic length scale of bicontinuous nanoporous structure by fast fourier transform, Jpn. J. Appl. Phys. **47**, 1161–1163 (2008)

21.106 T. Fujita, L.H. Qian, K. Inoke, J. Erlebacher, M.W. Chen: Three-dimensional morphology of nanoporous gold, Appl. Phys. Lett. **92**, 251902 (2008)

21.107 F.U. Renner, A. Stierle, H. Dosch, D.M. Kolb, T.L. Lee, J. Zegenhagen: In situ x-ray diffraction study of the initial dealloying and passivation of $Cu_3Au(111)$ during anodic dissolution, Phys. Rev. B **77**, 235433 (2008)

21.108 H. Rösner, S. Parida, D. Kramer, C.A. Volkert, J. Weissmüller: Reconstructing a nanoporous metal in three dimensions: An electron tomography study of dealloyed gold leaf, Adv. Eng. Mater. **9**, 535–541 (2007)

21.109 S.V. Petegem, S. Brandstetter, R. Maass, A.M. Hodge, B.S.E. Dasher, J. Biener, B. Schmitt, C. Borca, H. Van Swygenhoven: On the microstructure of nanoporous gold: An x-ray diffraction study, Nano Lett. **9**, 1158–1163 (2009)

21.110 Y. Sun, J. Ye, A.M. Minor, T.J. Balk: In situ indentation of nanoporous gold thin films in the transmission electron microscope, Microsc. Res. Technol. **72**, 232–241 (2009)

21.111 Y. Liu, S. Bliznakov, N. Dimitrov: Comprehensive study of the application of a Pb underpotential deposition-assisted method for surface area measurement of metallic nanoporous materials, J. Phys. Chem. C **113**, 12362–12372 (2009)

21.112 X.H. Gu, L.Q. Xu, F. Tian, Y. Ding: Au-Ag alloy nanoporous nanotubes, Nano Res. **2**, 386–393 (2009)

21.113 S.H. Yoo, S. Park: Platinum-coated, nanoporous gold nanorod arrays: Synthesis and characterization, Adv. Mater. **19**, 1612–1615 (2007)

21.114 T.Y. Shin, S.H. Yoo, S. Park: Gold nanotubes with a nanoporous wall: Their ultrathin platinum coating and superior electrocatalytic activity toward methanol oxidation, Chem. Mater. **20**, 5682–5686 (2008)

21.115 C.X. Xu, Y.Y. Li, F. Tian, Y. Ding: Dealloying to nanoporous silver and its implementation as a template material for construction of nanotubular mesoporous bimetallic nanostructures, ChemPhysChem **11**, 3320–3328 (2010)

21.116 X.G. Wang, W.M. Wang, Z. Qi, C.C. Zhao, H. Ji, Z.H. Zhang: Fabrication, microstructure and electrocatalytic property of novel nanoporous palladium composites, J. Alloy. Compd. **508**, 463–470 (2010)

21.117 Z. Qi, C.C. Zhao, X.G. Wang, J.K. Lin, W. Shao, Z.H. Zhang, X.F. Bian: Formation and characterization of monolithic nanoporous copper by chemical dealloying of Al-Cu alloys, J. Phys. Chem. C **113**, 6694–6698 (2009)

21.118 C.X. Xu, J.X. Su, X.H. Xu, P.P. Liu, H.J. Zhao, F. Tian, Y. Ding: Low temperature CO oxidation over unsupported nanoporous gold, J. Am. Chem. Soc. **129**, 42–43 (2007)

21.119 V. Zielasek, B. Jürgens, C. Schulz, J. Biener, M.M. Biener, A.V. Hamza, M. Bäumer: Gold catalysts:

Nanoporous gold foams, Angew. Chem. Int. Ed. **45**, 8241–8244 (2006)
21.120 C.X. Xu, X.H. Xu, J.X. Su, Y. Ding: Research on unsupported nanoporous gold catalyst for CO oxidation, J. Catal. **252**, 243–248 (2007)
21.121 D.Q. Han, T.T. Xu, J.X. Su, X.H. Xu, Y. Ding: Gas-phase selective oxidation of benzyl alcohol to benzaldehyde with molecular oxygen over unsupported nanoporous gold, ChemCatChem **2**, 383–386 (2010)
21.122 A. Wittstock, V. Zielasek, J. Biener, C.M. Friend, M. Bäumer: Nanoporous gold catalysts for selective gas-phase oxidative coupling of methanol at low temperature, Science **327**, 319–322 (2010)
21.123 M. Haruta: New generation of gold catalysts: Nanoporous foams and tubes – Is unsupported gold catalytically active?, ChemPhysChem **8**, 1911–1913 (2007)
21.124 A. Wittstock, B. Neumann, A. Schaefer, K. Dumbuya, C. Kübel, M.M. Biener, V. Zielasek, H.P. Steinrück, J.M. Gottfried, J. Biener, A. Hamza, M. Bäumer: Nanoporous Au: An unsupported pure gold catalyst?, J. Phys. Chem. C **113**, 5593–5600 (2009)
21.125 L.V. Moskaleva, S. Röhe, A. Wittstock, V. Zielasek, T. Klüner, K.M. Neyman, M. Bäumer: Silver residues as a possible key to a remarkable oxidative catalytic activity of nanoporous gold, Phys. Chem. Chem. Phys. **13**, 4529–4539 (2011)
21.126 H.M. Yin, C.Q. Zhou, C.X. Xu, P.P. Liu, X.H. Xu, Y. Ding: Aerobic oxidation of D-glucose on support-free nanoporous gold, J. Phys. Chem. C **112**, 9673–9678 (2008)
21.127 C.C. Jia, H.M. Yin, H.Y. Ma, R.Y. Wang, X.B. Ge, A.Q. Zhou, X.H. Xu, Y. Ding: Enhanced photoelectrocatalytic activity of methanol oxidation on TiO_2-decorated nanoporous gold, J. Phys. Chem. C **113**, 16138–16143 (2009)
21.128 Y.Y. Li, Y. Ding: Porous AgCl/Ag nanocomposites with enhanced visible light photocatalytic properties, J. Phys. Chem. C **114**, 3175–3179 (2010)
21.129 N. Asao, Y. Ishikawa, N. Hatakeyama, M. Menggenbateer, Y. Yamamoto, M.W. Chen, W. Zhang, A. Inoue: Nanostructured materials as catalysts: Nanoporous-gold-catalyzed oxidation of organosilanes with water, Angew. Chem. Int. Ed. **49**, 10093–10095 (2010)
21.130 J.T. Zhang, P.P. Liu, H.Y. Ma, Y. Ding: Nanostructured porous gold for methanol electrooxidation, J. Phys. Chem. C **111**, 10382–10388 (2007)
21.131 C. Yu, F. Jia, Z. Ai, L. Zhang: Direct oxidation of methanol on self-supported nanoporous gold film electrodes with high catalytic activity and stability, Chem. Mater. **19**, 6065–6067 (2007)
21.132 X. Ge, R. Wang, P. Liu, Y. Ding: Platinum-decorated nanoporous gold leaf for methanol electrooxidation, Chem. Mater. **19**, 5827–5829 (2007)
21.133 X. Ge, R. Wang, S. Cui, F. Tian, L. Xu, Y. Ding: Structure dependent electrooxidation of small organic molecules on Pt-decorated nanoporous gold membrane catalysts, Electrochem. Commun. **10**, 1494–1497 (2008)
21.134 J. Zhang, H. Ma, D. Zhang, P. Liu, F. Tian, Y. Ding: Electrocatalytic activity of bimetallic platinum–gold catalysts fabricated based on nanoporous gold, Phys. Chem. Chem. Phys. **10**, 3250–3255 (2008)
21.135 P. Liu, X. Ge, R. Wang, H. Ma, Y. Ding: Facile fabrication of ultrathin Pt overlayers onto nanoporous metal membranes via repeated Cu UPD and in situ redox replacement reaction, Langmuir **25**, 561–567 (2009)
21.136 R. Wang, C. Wang, W. Cai, Y. Ding: Ultralow-platinum-loading high-performance nanoporous electrocatalysts with nanoengineered surface structures, Adv. Mater. **22**, 1845–1848 (2010)
21.137 C.X. Xu, L. Wang, X.L. Mu, Y. Ding: Nanoporous PtRu alloys for electrocatalysis, Langmuir **26**, 7437 (2010)
21.138 M. Shao, K. Shoemaker, A. Peles, K. Kaneko, L. Protsailo: Pt monolayer on porous Pd-Cu alloys as oxygen reduction electrocatalysts, J. Am. Chem. Soc. **132**, 9253–9255 (2010)
21.139 S. Koh, P. Strasser: Electrocatalysis on bimetallic surfaces: Modifying catalytic reactivity for oxygen reduction by voltammetric surface dealloying, J. Am. Chem. Soc. **129**, 12624 (2007)
21.140 P. Mani, R. Srivastava, P. Strasser: Dealloyed Pt-Cu core-shell nanoparticle electrocatalysts for use in PEM fuel cell cathodes, J. Phys. Chem. C **112**, 2770–2778 (2008)
21.141 P. Strasser, S. Koha, J. Greeley: Voltammetric surface dealloying of Pt bimetallic nanoparticles: An experimental and DFT computational analysis, Phys. Chem. Chem. Phys. **10**, 3670–3683 (2008)
21.142 H.A. Gasteiger, S.S. Kocha, B. Sompalli, F.T. Wagner: Activity benchmarks and requirements for Pt, Pt-alloy, and non-Pt oxygen reduction catalysts for PEMFCs, Appl. Catal. B **56**, 9–35 (2005)
21.143 L. Liu, E. Pippel, R. Scholz, U. Gösele: Nanoporous Pt-Co alloy nanowires: Fabrication, characterization, and electrocatalytic properties, Nano Lett. **9**, 4352–4358 (2009)
21.144 L. Liu, R. Scholz, E. Pippel, U. Gösele: Microstructure, electrocatalytic and sensing properties of nanoporous $Pt_{46}Ni_{54}$ alloy nanowires fabricated by mild dealloying, J. Mater. Chem. **20**, 5621–5627 (2010)
21.145 L. Liu, Z. Huang, D. Wang, R. Scholz, E. Pippel: The fabrication of nanoporous Pt-based multimetallic alloy nanowires and their improved electrochemical durability, Nanotechnology **22**, 105604 (2011)
21.146 J. Snyder, T. Fujita, M.W. Chen, J. Erlebacher: Oxygen reduction in nanoporous metal–ionic liquid composite electrocatalysts, Nat. Mater. **9**, 904–907 (2010)

21.147 H.J. Herrmann, S. Roux: *Statistical Models for the Fracture of Disordered Media* (North-Holland, Amsterdam 1990)

21.148 R. Li, K. Sieradzki: Ductile-brittle transition in random porous Au, Phys. Rev. Lett. **68**, 1168–1171 (1992)

21.149 B. Kahng, G.G. Barttrouni, S. Redner, L. de Archangelis, H.J. Herrmann: Electrical breakdown in a fuse network with random, continuously distributed breakdown strengths, Phys. Rev. B **37**, 7625–7637 (1988)

21.150 J. Biener, A.M. Hodge, A.V. Hamza: Microscopic failure behavior of nanoporous gold, Appl. Phys. Lett. **87**, 121908 (2005)

21.151 J. Biener, A.M. Hodge, A.V. Hamza, L.M. Hsiung, J.H. Satcher: Nanoporous Au: A high yield strength material, J. Appl. Phys. **97**, 024301 (2005)

21.152 C.A. Volkert, E.T. Lilleodden, D. Kramer, J. Weissmüller: Approaching the theoretical strength in nanoporous Au, Appl. Phys. Lett. **89**, 061920 (2006)

21.153 A.M. Hodge, J.R. Hayes, J.A. Caro, J. Biener, A.V. Hamza: Characterization and mechanical behavior of nanoporous gold, Adv. Eng. Mater. **8**, 853–857 (2006)

21.154 A.M. Hodge, J. Biener, J.R. Hayes, P.M. Bythrow, C.A. Volkert, A.V. Hamza: Scaling equation for yield strength of nanoporous open-cell foams, Acta Mater. **55**, 1343–1349 (2007)

21.155 J. Biener, A.M. Hodge, J.R. Hayes, C.A. Volkert, L.A. Zepeda-Ruiz, A.V. Hamza, F.F. Abraham: Size effects on the mechanical behavior of nanoporous Au, Nano Lett. **6**, 2379–2382 (2006)

21.156 A. Mathur, J. Erlebacher: Size dependence of effective Young's modulus of nanoporous gold, Appl. Phys. Lett. **90**, 061910 (2007)

21.157 A.M. Hodge, R.T. Doucette, M.M. Biener, J. Biener, O. Cervantes, A.V. Hamza: Ag effects on the elastic modulus values of nanoporous Au foams, J. Mater. Res. **24**, 1600–1606 (2009)

21.158 D. Lee, X. Wei, X. Chen, M. Zhao, S.C. Jun, J. Hone, E.G. Herbert, W.C. Oliverd, J.W. Kysar: Microfabrication and mechanical properties of nanoporous gold at the nanoscale, Scr. Mater. **56**, 437–440 (2007)

21.159 D. Lee, X. Wei, M. Zhao, X. Chen, S.C. Jun, J. Hone, J.W. Kysar: Plastic deformation in nanoscale gold single crystals and open-celled nanoporous gold, Model. Simul. Mater. Sci. Eng. **15**, S181–S192 (2007)

21.160 E. Seker, J.T. Gaskins, H. Bart-Smith, J. Zhu, M.L. Reed, G. Zangari, R. Kelly, M.R. Begley: The effects of post-fabrication annealing on the mechanical properties of freestanding nanoporous gold structures, Acta Mater. **55**, 4593–4602 (2007)

21.161 E. Seker, J.T. Gaskins, H. Bart-Smith, J. Zhu, M.L. Reed, G. Zangari, R. Kelly, M.R. Begley: The effects of annealing prior to dealloying on the mechanical properties of nanoporous gold microbeams, Acta Mater. **56**, 324–332 (2008)

21.162 H. Jin, L. Kurmanaeva, J. Schmauch, H. Rösner, Y. Ivanisenko, J. Weissmüller: Deforming nanoporous metal: Role of lattice coherency, Acta Mater. **57**, 2665–2672 (2009)

21.163 H. Jin, J. Weissmüller: A material with electrically tunable strength and flow stress, Science **332**, 1179–1182 (2011)

21.164 A.I. Maaroof, M.B. Cortie, G.B. Smith: Optical properties of mesoporous gold films, J. Opt. A **7**, 303–309 (2005)

21.165 A.I. Maaroof, A. Gentle, G.B. Smith, M.B. Cortie: Bulk and surface plasmons in highly nanoporous gold films, J. Phys. D **40**, 5675–5682 (2007)

21.166 F. Yu, S. Ahl, A.-M. Caminade, J.-P. Majoral, W. Knoll, J. Erlebacher: Simultaneous excitation of propagating and localized surface plasmon resonance in nanoporous gold membranes, Anal. Chem. **78**, 7346–7350 (2006)

21.167 S. Ahl, P.J. Cameron, J. Liu, W. Knoll, J. Erlebacher, F. Yu: A comparative plasmonic study of nanoporous and evaporated gold films, Plasmonics **3**, 13–20 (2008)

21.168 L. Qian, W. Shen, B. Das, B. Shen, G.W. Qin: Alumina coating of ultrafine nanoporous gold at room temperature and their optical properties, Chem. Phys. Lett. **479**, 259–263 (2009)

21.169 L. Qian, W. Shen, B. Shen, G.W. Qin, B. Das: Nanoporous gold–alumina core–shell films with tunable optical properties, Nanotechnology **21**, 305705 (2010)

21.170 S.O. Kucheyev, J.R. Hayes, J. Biener, T. Huser, C.E. Talley, A.V. Hamza: Surface-enhanced Raman scattering on nanoporous Au, Appl. Phys. Lett. **89**, 053102 (2006)

21.171 M.C. Dixon, T.A. Daniel, M. Hieda, D.M. Smilgies, M.H.W. Chan, D.L. Allara: Preparation, structure, and optical properties of nanoporous gold thin films, Langmuir **23**, 2414–2422 (2007)

21.172 L.H. Qian, X.Q. Yan, T. Fujita, A. Inoue, M.W. Chen: Surface enhanced Raman scattering of nanoporous gold: Smaller pore sizes stronger enhancements, Appl. Phys. Lett. **90**, 153120 (2007)

21.173 L.H. Qian, A. Inoue, M.W. Chen: Large surface enhanced Raman scattering enhancements from fracture surfaces of nanoporous gold, Appl. Phys. Lett. **92**, 093113 (2008)

21.174 X.Y. Lang, L.Y. Chen, P.F. Guan, T. Fujita, M.W. Chen: Geometric effect on surface enhanced Raman scattering of nanoporous gold: Improving Raman scattering by tailoring ligament and nanopore ratios, Appl. Phys. Lett. **94**, 213109 (2009)

21.175 X.Y. Lang, P.F. Guan, L. Zhang, T. Fujita, M.W. Chen: Characteristic length and temperature dependence of surface enhanced Raman scattering of nanoporous gold, J. Phys. Chem. C **113**, 10956–10961 (2009)

21.176 L.-Y. Chen, J.-S. Yu, T. Fujita, M.-W. Chen: Nanoporous copper with tunable nanoporosity for SERS applications, Adv. Funct. Mater. **19**, 1221–1226 (2009)

21.177 L.Y. Chen, L. Zhang, T. Fujita, M.W. Chen: Surface-enhanced Raman scattering of silver@nanoporous copper core-shell composites synthesized by an in situ sacrificial template approach, J. Phys. Chem. C **113**, 14195–14199 (2009)

21.178 L.H. Qian, B. Das, Y. Li, Z. Yang: Giant Raman enhancement on nanoporous gold film by conjugating with nanoparticles for single-molecule detection, J. Mater. Chem. **20**, 6891–6895 (2010)

21.179 X.Y. Lang, P.F. Guan, L. Zhang, T. Fujita, M.W. Chen: Size dependence of molecular fluorescence enhancement of nanoporous gold, Appl. Phys. Lett. **96**, 073701 (2010)

21.180 X.Y. Lang, P.F. Guan, T. Fujita, M.W. Chen: Tailored nanoporous gold for ultrahigh fluorescence enhancement, Phys. Chem. Chem. Phys. **13**, 3795–3799 (2011)

21.181 C.-H. Chou, J.-C. Chen, C.-C. Tai, I.-W. Sun, J.-M. Zen: A nonenzymatic glucose sensor using nanoporous platinum electrodes prepared by electrochemical alloying/dealloying in a water-insensitive zinc chloride-1-ethyl-3-methylimidazolium chloride ionic liquid, Electroanalysis **20**, 771–775 (2008)

21.182 Z. Liu, J. Du, C. Qiu, L. Huang, H. Ma, D. Shen, Y. Ding: Electrochemical sensor for detection of p-nitrophenol based on nanoporous gold, Electrochem. Commun. **11**, 1365–1368 (2009)

21.183 H. Qiu, C. Xu, X. Huang, Y. Ding, Y. Qu, P. Gao: Adsorption of laccase on the surface of nanoporous gold and the direct electron transfer between them, J. Phys. Chem. C **112**, 14781–14785 (2008)

21.184 H. Qiu, L. Lu, X. Huang, Z. Zhang, Y. Qu: Immobilization of horseradish peroxidase on nanoporous copper and its potential applications, Bioresource Technol. **10**, 19415–19420 (2010)

21.185 X. Ge, L. Wang, Z. Liu, Y. Ding: Nanoporous gold Leaf for amperometric determination of nitrite, Electroanalysis **23**, 381–386 (2011)

21.186 J. Biener, A. Wittstock, L.A. Zepeda-Ruiz, M.M. Biener, V. Zielasek, D. Kramer, R.N. Viswanath, J. Weissmüller, M. Bäumer, A.V. Hamza: Surface-chemistry-driven actuation in nanoporous gold, Nat. Mater. **8**, 47–51 (2009)

21.187 H.-J. Jin, X.-L. Wang, S. Parida, K. Wang, M. Seo, J. Weissmüller: Nanoporous Au-Pt alloys as large strain electrochemical actuators, Nano Lett. **10**, 187–194 (2010)

21.188 A.K. Mishra, C. Bansal, H. Hahn: Surface charge induced variation in the electrical conductivity of nanoporous gold, J. Appl. Phys. **103**, 094308 (2008)

21.189 T. Fujita, H. Okada, K. Koyama, K. Watanabe, S. Maekawa, M.W. Chen: Unusually small electrical resistance of three-dimensional nanoporous gold in external magnetic fields, Phys. Rev. Lett. **101**, 166601 (2008)

21.190 R. Xia, J.L. Wang, R. Wang, X. Li, X. Zhang, X.-Q. Feng, Y. Ding: Correlation of the thermal and electrical conductivities of nanoporous gold, Nanotechnology **21**, 085703 (2010)

21.191 P. Wahl, T. Traußnig, S. Landgraf, H.-J. Jin, J. Weissmüller, R. Würschum: Adsorption-driven tuning of the electrical resistance of nanoporous gold, J. Appl. Phys. **108**, 073706 (2010)

21.192 M. Hakamada, M. Takahashi, T. Furukawa, M. Mabuchi: Coercivity of nanoporous Ni produced by dealloying, Appl. Phys. Lett. **94**, 153105 (2009)

21.193 M. Hakamada, M. Takahashi, T. Furukawa, M. Mabuchi: Surface effects on saturation magnetization in nanoporous Ni, Philos. Mag. **90**, 1915–1924 (2010)

21.194 R. Zeis, A. Mathur, G. Fritz, J. Lee, J. Erlebacher: Platinum-plated nanoporous gold: An efficient, low Pt loading electrocatalyst for PEM fuel cells, J. Power Sources **165**, 65–72 (2007)

21.195 X. Lang, A. Hirata, T. Fujita, M. Chen: Nanoporous metal/oxide hybrid electrodes for electrochemical supercapacitors, Nat. Nanotechnol. **6**, 232–236 (2011)

21.196 Z. Liu, P.C. Searson: Single nanoporous gold nanowire sensors, J. Phys. Chem. B **110**, 4318–4322 (2006)